International Journal of Fatigue 206 (2026) 109447

Contents lists available at ScienceDirect

International Journal of Fatigue

journal homepage: www.elsevier.com/locate/ijfatigue

Fatigue performance of Ti6Al4V lattices: relative density as a partial quantitative predictor

Pietro Foti [a,b], Asghar Heydari Astaraee [c], Sara Bagherifard [c], Anton du Plessis [d,e], Di Wan [a,f], Filippo Berto [a,b], Nima Razavi [a,*]

[a] Department of Mechanical and Industrial Engineering, Norwegian University of Science and Technology (NTNU), Richard Birkelands vei 2B, 7491 Trondheim, Norway
[b] Department of Chemical, Material and Environmental Engineering (DICMA), La Sapienza University of Rome, Via Eudossiana 18, 00184 Rome, Italy
[c] Department of Mechanical Engineering, Politecnico di Milano, Via L Masa 1, 20156 Milan, Italy
[d] Math2Market North America Inc., Atlanta, United States
[e] Stellenbosch University, Stellenbosch, South Africa
[f] School of Interdisciplinary Science, Beijing Institute of Technology, Zhongguancun South Street 5, 100081 Beijing, China

ARTICLE INFO

Keywords:
Fatigue
Additive manufacturing
Lattice
Ti6Al4V
Relative density

ABSTRACT

Lattice structures realized through additive manufacturing have garnered increasing interest within both academia and industry in recent years. Various factors, including unit cell topology, base material, heat treatments, and relative density, significantly influence the overall behaviour of these architectured structures. This study specifically examines the compressive mechanical behaviour of solid-based gyroid lattices made of Ti6Al4V alloy through Laser Powder Bed Fusion (PBF-LB) technique. Specimens with four different relative densities were produced to investigate the impact of this parameter on the compressive behaviour (quasi-static and fatigue); furthermore, each relative density category included two sets of specimens to evaluate the effect of annealing and Hot Isostatic Pressing (HIP) as post-processing techniques. Micro-CT scans, microstructural, postmortem and finite element analyses were included to further evaluate the failure mechanisms and explain the observed experimental results. Furthermore, the behaviour documented in the present analysis has been correlated with a wide fatigue dataset retrieved from literature in an effort to dig deeper into the behaviour of these structures. The results, together with the retrieved dataset, allowed for a more comprehensive understanding also considering aspects such as yielding effect, surface roughness and notch mechanics. It has been proved that the use of optimized process parameters and cheaper heat treatments is able to match the beneficial effects expected by HIP. Furthermore, easy-to-use methodologies to account for the reduction in strength due to the change in relative density presented in the literature, such as effective and normalized stress, have been considered to evaluate their accuracy, but also their limitations.

1. Introduction

Conventional manufacturing struggles to meet the demand for customized components and the full exploitation of material properties, limiting the production of innovative, lightweight designs. Additive manufacturing (AM) overcomes these constraints, unlocking opportunities to customize component properties that were previously unattainable. This is particularly evident in lattice structures and multi-topology metamaterials [1]. Lattice structures consist of periodic unit cells whose design parameters govern the global mechanical behaviour. Despite the vast potential for global design variations, only a few unit cell configurations meet the requirement for a regular and undistorted periodic pattern [2,3]. Among these, triply periodic minimal surface (TPMS) lattices are particularly appreciated in biomedical applications due to their biomorphic, interconnected porous geometries that promote tissue integration and mass transport [4–7]. The mechanical behaviour of AM lattice components is strongly influenced by both manufacturing conditions [8–10] and geometrical features [11–13]. Process-induced defects, residual stresses, anisotropy and surface quality – that depends also on the surface orientation with respect to the building one [14] – significantly affect their mechanical performance. However, the influence of individual process parameters remains difficult to isolate

* Corresponding author.
E-mail address: nima.razavi@ntnu.no (N. Razavi).

https://doi.org/10.1016/j.ijfatigue.2025.109447
Received 4 August 2025; Received in revised form 11 December 2025; Accepted 14 December 2025
Available online 16 December 2025

[15–17].

A key parameter controlling the overall lattice behaviour is the relative density, defined as the ratio of actual material volume and total component volume [3,11]. Considering lattices as metamaterials, in terms of nominal stress values – given by the ratio of load and gross section of lattice component, a fatigue strength decrease must be expected with a decrease in the relative density: a smaller strut net cross-section leads to lower critical loads having the maximum critical stress limited by the bulk material properties. Foreseeing the degree of this reduction in fatigue strength is not straightforward. Various attempts have been done to establish easy-to-use design methodologies to account for such strength variation. One of the proposed solutions is the so-called effective stress, defined as the nominal stress divided by the relative density of the component analysed. Although evidence in the literature suggests that this may be a valid solution to account for the effect of relative density [18], counterproofs weaken and restrain its validity [19], proving that its applicability must be established at least on the basis of additional conditions. Indeed, the same value of relative density can be achieved through different combinations of unit cell size and strut thicknesses. By changing the latter one while keeping constant the process parameters, various outcomes can be obtained in terms of micro-porosity, microstructure and ratio between the strut/wall thickness and the surface features [19], leading to possible influences on the achieved mechanical properties.

An alternative is the normalized fatigue strength [11], the ratio of fatigue to yield strengths of the component. Proofs have been provided in literature to support the hypothesis that relating the fatigue strength to the quasi-static mechanical properties may allow accounting for various parameters such as material, microstructure, real geometry, and of course, relative density [11]. Although its validity appears to be strengthened by its overall satisfying application in various works [20–24], the comparison of such results reveals dependencies from aspects, such as the unit cell geometry, that, according to the method hypothesis, should already be accounted for. Appropriate and in-depth discussions on this topic will be provided within dedicated sections in this work. Dealing with AM, proper comparison on this basis requires minimizing variations in other possible influencing factors such as the process parameters. However, relationships between quasi-static and fatigue behaviour represented the scope of much research carried out also on conventional components and materials, resulting in promising, yet not conclusive, solutions. Despite the importance and value of the most recent research, well-established and consolidated outcomes from decades of research work on fatigue often end up being overlooked; among these, the yielding effect, surface roughness effect and notch mechanics [18] may provide promising points of view to explain the differences in the fatigue behaviour of lattice components available in literature.

Among the various methodologies used to investigate the mechanical behaviour of lattices – particularly their fatigue performance – local approaches may represent a valuable solution. In the literature, the term “local” has been employed to describe methods of different nature. For instance, Meshram et al. [25] used it to denote a point method (specifically as “local stress”) that evaluates the maximum stress in trusses simplified as beams, while neglecting features such as the nodes at strut intersections, which are responsible for stress concentrations and gradients. Conversely, other studies – such as those by Raghavendra et al. [26], De Biasi et al. [27] and Boniotti et al. [28] – adopt methodologies typically referred to as local approaches in literature, specifically the averaged strain energy density (SED) method [26,27] and the theory of critical distances (TCD) combined with the von Mises stress [28]. These field-based local approaches directly account for the effects of stress concentrations and gradients arising from the notches created by struts intersections. Furthermore, the application of fracture mechanics concepts to the fatigue assessment of lattices has also been explored, for example, by Collini and Meneghetti [29].

Limited research efforts are usually dedicated to interpreting the observed experimental behaviour in a wider perspective, confining the analysis to the boundaries of the variables directly studied. Yet, many works have significantly contributed to exploring ways to improve lattice fatigue performance. A major limitation of AM is the high occurrence of internal and surface defects [30] whose reduction enhances the fatigue performance. Studies investigating lattices with different relative densities obtained through different wall thicknesses reported varying fatigue responses and levels of micro-porosity [19], suggesting a cause-and-effect relationship. Moving from these and similar observations, post-treatments aimed at reducing internal porosity have been investigated to improve and homogenize fatigue performance across different relative densities. Several post-processing treatments have been explored to mitigate inherent AM defects that persist despite optimized process parameters being employed. Mechanical and chemical treatments improve surface quality [31–35] while other methods address internal defects and microstructural issues [13,36,37]. Among them, Hot Isostatic Pressing (HIP) reduces internal porosity, residual stresses, and anisotropy [38,39] while improving ductility in Ti6Al4V, though reducing the yield strength [40]. HIP generally improves fatigue performance and reduces data scatter [41–43] acting on the internal microporosity; therefore, its benefits may be limited in lattice structures, where fatigue is often surface-driven and surface finishing is challenging [44–46]. Nevertheless, its microstructural benefits remain of interest, although simpler and cheaper post-treatments may offer comparable improvements.

Various parameters influence lattices fatigue behaviour, making their experimental assessment challenging due to possible synergistic effects. Moreover, features such as defects, surface roughness and geometrical deviations must be properly quantified to be accounted for; X-ray microcomputed tomography (micro-CT) is widely used for their characterization [47–53] while finite element (FE) analysis is commonly adopted as a complementary tool to investigate their effect through micro-CT reconstructed geometries [54,55]. Nevertheless, numerical predictions still fail to fully capture the experimental behavior; the reasons for this may be diverse but examining them could also help clarify the limitations that affect this investigation procedure. Discrepancies between numerical and experimental results could be attributed to several factors, including residual stresses, microstructural anisotropy, but also technical limitations in FE modelling, such as meshing simplification that may have decreased the severity of surface notches [56]. Moreover, a key role is played by the assumed failure hypothesis that may not adequately represent the actual fatigue mechanism or regime under analysis [28]. For instance, sharp surface-induced notches often invalidate point-based fatigue approaches with fracture mechanics (FM) being more suitable; yet FM hypothesis may be violated due to the limited dimensions of the strut/wall thickness. As a result, unavoidable simplifying assumptions limit a fully comprehensive description of AM lattice behaviour through FE analyses alone. Despite these limitations, FE modeling remains essential to efficiently explore large design spaces, allowing preliminary numerical screening before experimental validation. Moreover, explicitly modelling all possible influencing aspects is neither feasible nor always advisable as poorly quantified effects may still lead to wrong conclusions while marginal contributions, such as surface roughness in quasi-static loading, may drastically increase computational cost with minimal accuracy gains. Leaving aside all the discussions about its accuracy, FE analysis still provides valuable insight into stress distribution and failure initiation in lattice structures [57–59], even when based only on as-designed geometries.

This study presents a systematic analysis of the mechanical properties of solid gyroid lattices under quasi-static and fatigue loading conditions, focusing primarily on the effect of relative density and post-treatment techniques on their mechanical response. In addition to examining the relationship between design, printing outcome, and mechanical performance, the potential benefits of HIP have been evaluated to determine the extent of its impact across the cases considered. As a secondary objective of the present study, this evaluation aims to

establish whether comparable benefits to those achieved with HIP treatment can be attained using less expensive and less complex techniques. The analysis is further supported by microstructural and post-mortem analyses and FE simulations. Finally, a more complete overview of the fatigue behaviour of lattices is attempted, considering also data drawn from literature in an effort to enclose the fatigue behaviour documented in the present work in a broader one that could also exhaustively explain all the considered fatigue data.

2. Materials and methods

2.1. Specimens design and fabrication

Solid-based gyroid lattices made of Ti6Al4V alloys were produced through PBF-LB process with the EOS M290 system using the default prescribed parameters for this material (i.e.: laser power of 280 W; scan speed of 1200 mm/s; 0.14 mm hatch spacing; 0.03 mm layer height and hatch scanning performed with a zig-zag fashion with 67° rotation on each layer followed by a contour scanning). Lattice coupon specimens were fabricated with nominal relative densities of 12.5 %, 25 %, 37.5 % and 50 %. The mathematical models of gyroids can be obtained through approximate level-set equations [60] that have the following expressions:

$$\sin\left(\frac{2\pi}{a}\cdot x\right)\cdot\cos\left(\frac{2\pi}{a}\cdot y\right)+\sin\left(\frac{2\pi}{a}\cdot y\right)\cdot\cos\left(\frac{2\pi}{a}\cdot z\right)+\sin\left(\frac{2\pi}{a}\cdot z\right)\cdot\cos\left(\frac{2\pi}{a}\cdot x\right)=c$$

where x, y and z are the spatial coordinates in a Cartesian coordinate system, while a controls the unit cell size and c the porosity of the cell. The designs were created using nTop software [61] and representative images are shown in Fig. 1 with changing the relative density.

Each specimen was composed of five unit-cells of 4 mm size per side along each direction, resulting in a cubic specimen size of 20 mm. After the production, all specimens were stress relieved (SR) (in a vacuum furnace for 3 h at 650 °C prior to removal from the baseplate) and annealed (ANN) (in vacuum for 2 h in an annealing soak at 940 °C). Subsequently, the specimens were divided into two groups. One group underwent HIP at Quintus Technologies AB (Sweden) in Argon at 100 MPa with a 2 h soak time at 925 °C, followed by a slow cooling of ~−10 °C/min. This specific combination of post-treatments was selected in an attempt to decouple the effects of microstructure and microporosity. The resulting microstructure was expected to be primarily governed by the ANN process, while the subsequent HIP treatment, performed at a slightly lower temperature than ANN, was intended to act mainly on microporosity without significantly affecting the microstructure. Detailed discussions of these aspects are provided in the Results and Discussions subsections.

For clarity, the treatment conditions considered in the present work are denoted as ANN for stress-relieved and annealed specimens and ANN-HIP for stress-relieved, annealed and HIPed specimens.

2.2. Micro-CT scan

Micro-CT scans were performed using a GE Nanotom S system. To scan the entire samples 150 kV and 130 μA were used, with a 0.5 mm copper beam filter, and 3000 images per full rotation to obtain a 14 μm voxel size. The micro-CT data have been post-processed using the software Dragonfly 3D World 2024.1.

The micro-CT data were used to reconstruct the actual geometry of the printed components and to evaluate wall thickness, deviation from the as-designed geometry and actual relative density. The segmentation was performed using thresholding and wall thickness was determined using the mesh thickness function. Deviations were calculated by registration of the design mesh to the actual mesh and applying a signed-deviation mapping function. In both cases, statistical analysis was performed directly within Dragonfly 3D World software.

2.3. Experimental campaign

Scanning Electron Microscopy (SEM) was performed using a Thermo Fisher Quanta™ 650 FEG with 20 kV accelerating voltage. The samples extracted for the microstructure analysis were ground down to 4000 grit and electropolished using a methanolic H_2SO_4 (1 mol/L) electrolyte at 35 V for 60 s. Electron Backscattered Diffraction (EBSD) was carried out at a working distance of 20 mm, a step size of 0.5 μm in areas of 200 μm × 200 μm to determine the grain size distribution and Pole figures using an orientation imaging microscopy system attached to the SEM system.

Quasi-static compression tests were performed on two specimens per condition at a displacement rate of 1 mm/min using an MTS Alliance RT/150 machine. The tests were ended after reaching at least 1.3 times the first peak load; although neglecting the densification phase of the curve in some cases, this approach ensured the evaluation of all the mechanical properties in accordance with ISO-13314 standard [62]. The bulk material was characterized through uniaxial tensile testing on vertically printed dog-bone specimens in the ANN condition, following ISO 6892-1 [63], on an MTS Alliance RT/100 machine at room temperature and a displacement rate of 1 mm/min. Uniaxial compression fatigue tests were performed on lattice specimens using an MTS 100 kN Axial-Torsion Machine under load control at a frequency of 20 Hz and a load ratio of 0.1 in compression (intended as the ratio between the minimum and maximum load magnitudes, irrespective of their negative signs). The loading direction coincided with the building direction of the specimens to avoid possible influence given by surface roughness variations between differently oriented surfaces of the specimens (such as, for example, down-skin regions). The tests were ended when either a global strain of 20 % was reached or 2 million cycles were completed without failure. Notably, the chosen strain limit does not influence the outcomes achieved as the specimens may be assumed fully collapsed at this condition [64]. Indeed, in high-cycle fatigue, the maximum compressive strain can be assumed to remain constant for most of the fatigue life with a sudden increase right before the final collapse [64]. Therefore, although arbitrary, the chosen ending condition does not significantly influence the number of cycles to failure, as the sudden increase of strain happens in a very limited part of the total fatigue life.

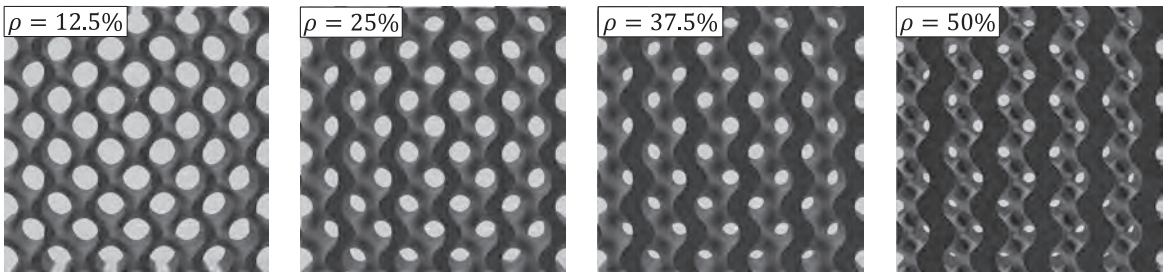

Fig. 1. Schematic representation of the studied specimens.

Furthermore, such a value of global strain allows postmortem analysis as the specimens are not completely crushed. The fatigue data were analysed assuming a linear relation in a log–log S-N diagram to determine the inverse slope, the scatter band for probabilities of survival (PS) of 10 %, 50 % and 90 % and the scatter index (defined as the ratio between the fatigue strength value at 2 million cycles for 10 % PS over the one at 90 %PS).

The failed specimens were then prepared to investigate the fatigue fracture morphology and the failure mechanism using SEM. The specimens were prepared through ultrasonic cleaning in ethanol for five minutes to remove nonconductive particles such as dust.

2.4. FE model

3D modelling and simulation were carried out in ABAQUS/Explicit 2019 on the lattice specimens (with a cube size of 20 mm) at all the investigated relative densities. An explicit solver was chosen due to its high robustness and efficiency in solving highly non-linear quasi-static problems. The representative numerical model is shown in Fig. S1(a). The CAD lattice geometries (STL) were meshed in Altair HyperWorks software 2023 using the shrink-wrap algorithm and 3D cubic hexahedral 8-node elements with reduced integration (C3D8R). Element sizes of 0.1, 0.125, 0.135, and 0.15 mm were used for the respective relative densities (12.5 %, 25 %, 37.5 % and 50 %), ensuring sufficient refinement relative to the wall thickness. Larger elements at higher relative densities reduced computational time while maintaining an approximately constant number of elements through the wall thickness. The meshed domain was then imported into Abaqus for further model development. Analytical rigid surfaces were used to represent the upper and lower plates, reproducing the experimental setup.

The material properties of bulk annealed PBF-LB Ti6Al4V, listed in Table 1, were applied in the FE model. The quasi-static behavior of the bulk material, obtained from uniaxial tensile testing on dog-bone samples, is shown in Fig. S1b). Damage initiation and damage evolution were modeled using the plastic strain-based Johnson-Cook model ($\bar{\varepsilon}_0^{pl}$), available in Abaqus Explicit:

$$\bar{\varepsilon}_0^{pl} = [D_1 + D_2 \exp(D_3 \sigma^*)][1 + D_4 \ln(\dot{\varepsilon}^*)][1 + D_5 T^*]$$

where σ^* is the stress triaxiality, $\dot{\varepsilon}^*$ is the strain rate, T^* is the homologous temperature, and D_1 to D_5 are material constants. These constants, reported in Table 1, were adopted from [65], which was developed specifically for annealed PBF-LB Ti6Al4V. For quasi-static compression tests at room temperature, D_4 and D_5 were set to zero. Progressive failure was defined based on the fracture energy per unit area, G_f, which depends on the material fracture toughness and geometrical conditions (i.e., plane stress or plane strain). Its selection is discussed in the results section.

All degrees of freedom of the plates were constrained, except for the vertical translation of the upper plate along the Y-axis to impose the compression displacement. The boundary conditions were applied via reference points assigned to the rigid plates. Interactions, including self-contact even after element deletion due to damage evolution, were modeled using tangential contact behavior with a penalty formulation and a friction coefficient of 0.2 [66]. To achieve reasonable computational efficiency, time scaling was applied by increasing the test speed to 0.015 mm/s. The kinetic energy was monitored to ensure it remained a negligible fraction of the internal energy. Further details can be found in [67].

The model was developed to investigate the deformation behavior and the stress field, providing insights into the observed failure mechanisms and identifying the critical locations leading to failure.

Table 1
Physical and mechanical properties of PBF-LB Ti6Al4V.

Material property	Unit	Value	Ref
Density	g/cm^3	4.42	[68]
Elastic modulus	GPa	111	[68]
Poisson's ratio	–	0.3	[68]
Yield strength	MPa	833	Current work
Ultimate tensile strength	MPa	911	Current work
Elongation	%	19.4	Current work
Material constant D_1	–	−0.68	[65]
Material constant D_2	–	0.73	[65]
Material constant D_3	–	−0.25	[65]

3. Results and discussions

3.1. Micro-CT scan

The actual geometry was reconstructed from micro-CT scans of the printed specimens at the various relative densities investigated. The primary objective was to assess the geometrical deviation of the printed parts from their original designs and to evaluate whether a dependency on the feature size exists as a function of design relative density. Additionally, the micro-CT data were used to support the discussions on the failure mechanisms with different relative densities. The results are presented as 3D and frontal 3D renderings as well as diagrams quantifying the measured wall thickness and deviations between actual and as-designed geometries. Microporosity measurements were also performed, revealing that the optimized process parameters resulted in a microporosity level below the detection threshold of the micro-CT scans.

Fig. 2(a) shows the as-designed geometries of the investigated specimens at the various relative densities, while Fig. 2(b) reports the corresponding actual geometries; the colour maps represents the wall thickness. The actual geometry presents a non-uniform wall thickness across the specimens. However, part of this variation must not be addressed to the AM process as it originates from the design itself; as visible in Fig. 2(a), they are expected also in the as-designed specimens due to the outer borders (geometry boundaries). Fig. 2(c) reports a frontal view in which the variation in wall thickness caused solely by the printing process could be better appreciated. Small gradients in wall thickness appear between the ligaments, presenting a lower thickness than the intersections (notice the magnifications reported). This is more evident with higher relative densities. Overall, such variations are limited, as confirmed by the wall thickness histogram in Fig. 2(e). Disregarding the left tail of the frequency distribution, such variations probably contribute to the nearly symmetrical and narrow band around the mode value. The smaller wall thickness values constituting the left tail of the histogram, presenting also low frequencies, should correspond to the specimens' borders, as visible in Fig. 2(a) and (b), where regions of lower thicknesses occur at the specimens' borders. Fig. 2(d) shows a nominal-actual comparison through a frontal 3D rendering of deviations from the as-designed geometry. These images further prove that the larger wall thickness changes observed in Fig. 2(b) mainly stem from the as-designed geometry itself rather than the manufacturing process. Furthermore, the magnified views also reveal that most of the deviations are due to excess overhanging material on down-skin surfaces and to the typical roughness of AM components. Moreover, negative deviations, related to thinner regions, generally occur at the ligaments while positive ones, related to thicker one, occur at the intersection, as confirmed by the deviation histogram in Fig. 2(e), which is approximately symmetrical about the zero-deviation axis.

All the deviations recorded in the actual geometry resulted in different wall thickness and relative density between the as-designed and actual specimens, summarized in Table 2 (as regards the wall thickness, the mode value of its distribution is reported). Although all the analysed samples show an overall reduction in their wall thickness mode, the measured relative densities are higher than their as-designed values. The higher left tail of the wall thickness frequency distribution with respect to the as-designed one suggests that, although a lower relative density was probably achieved in the core of the specimen, the

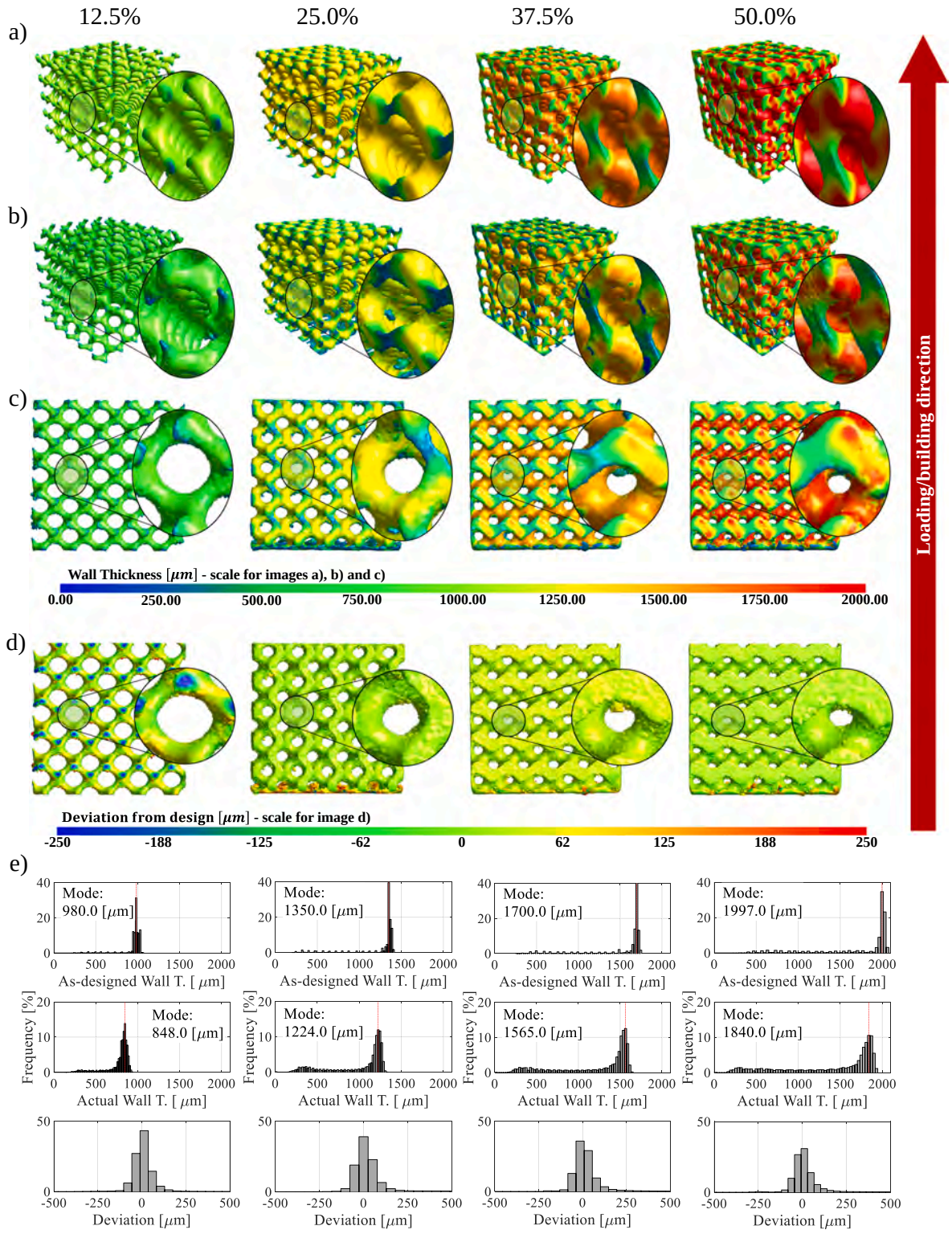

Fig. 2. (a) As-designed geometries; (b) micro-ct-based 3d reconstruction; (c) micro-ct-based frontal 3d reconstruction; (d) frontal 3d renderings showing actual vs as-design deviations colour map; (e) histograms of wall thickness for as-designed (top) and actual (middle) geometries and deviation (bottom) at different relative densities.

average value is severely affected by deviation at its outer surface. The largest discrepancy in relative density was observed in the sample with an as-designed value of 25 %; Fig. 2(d) reveals that the higher deviations occur at its bottom surface, supporting the assumption that the measured relative density is strongly influenced by border effects. Consequently, the measured the actual relative density may, in some cases, not be representative of the actual one in the core of the specimen.

3.2. Microstructural analysis

The microstructure of the produced samples in the plane perpendicular to the build direction (XY plane according to the ISO/ASTM

Table 2
As-designed versus actual values of relative densities and wall thickness.

Relative density			Wall Thickness (mode value)		
As-designed	Actual	Difference as-designed vs actual	As-designed	Actual	Difference as-designed vs actual
[%]	[%]	[%]	[μm]	[μm]	[%]
12.5	13.3	6.4	980	848	−13.5
25	27.7	10.8	1350	1224	−9.3
37.5	39.4	5.07	1700	1565	−7.9
50	51.4	2.8	1997	1840	−7.9

52,900 standard [69]) was investigated through SEM.

EBSD experiments were performed to investigate the grain distribution and size to assess possible anisotropic features and microstructural differences between the two analysed conditions – i.e. ANN and ANN-HIP. Only the α-Ti phase was identified and indexed for the EBSD scans. The microstructure of the specimens is revealed by the building direction – inverse pole figure (BD-IPF) maps (Fig. 3). No significant variations were noticed between the ANN and ANN-HIP conditions, including the crystallographic texture (see Fig. S2), grain size distribution (see Fig. S3), and residual strain levels (through kernel average misorientation maps in Fig. S4). Furthermore, the porosity between the edge and the central part of each strut did not show distinct differences for each single fabricated specimen. The microstructure of the fabricated specimens is relatively stable with regard to the applied treatments.

3.3. Quasi-static compressive behaviour

Fig. 4 reports the quasi-static compression behaviour of the specimens printed with different relative densities for both ANN (see Fig. 4 (a)) and ANN-HIP (see Fig. 4(b)) conditions. Due to the complex geometry of the coupon specimens studied, the definition of stress and strain considered for the quasi-static analysis in the present work follows the standard ISO-13314:2011 [62]. Specifically, the stress considered is the nominal stress, defined as $\sigma_{nominal} = Load/A_{gross}$ where A_{gross} is the gross section of the specimens while the nominal strain is obtained by the overall compressive displacement divided by the initial specimen height.

As shown in Fig. 4(a) and(b), the first initial elastic response is followed by a long plateau before entering the densification stage characterized by a further increase in stress. The densification region is reached at different nominal strains depending on the relative density. Assuming no dimensional variations along the transverse directions, complete densification would be reached for lower global nominal strain values with increasing the relative density. Furthermore, the fluctuations in the plateau region would appear to be smaller with decreasing the specimen relative density. When normalizing the stress by the first peak value along the plateau region, as in Fig. 4(c) and(d), the overall behaviour at different relative densities is comparable once if considerations regarding the different maximum nominal strains to full densification are kept in mind. At each relative density a clear drop in the strength of about 50 % of the first peak stress occurs within similar nominal strain values. A closer look, in Fig. 4(e) and (f), reveals that the overall appearance of this strength drop depends on the relative density; at lower relative densities, the drop is gradual, while at the highest relative density (50 %) it appears abrupt. Such drops in strength in the plateau region have been observed both in bending-dominated and in stretching-dominated lattices [70–73]. Various phenomena can occur within the plateau region, such as elastic and inelastic buckling, plastic collapse, or strut/ligament fracture depending on various conditions [74].

A first interpretation could attribute the strength drop to buckling leading to the collapse of a single layer (or of cells along peculiar directions), to which a further increase in strength would follow. However, the strength drops in this work also affect higher relative densities, where the lower slenderness would make the occurrence of buckling less likely. Furthermore, the characteristic trends observed do not agree well with such a phenomenon. Referring to other works specifically dealing with buckling [75,76], it can be observed that if buckling occurs, with increasing the strut/wall thickness, the drop in strength is lower and more gradual. Gumruk et al. [77] reported similar strength drops for both F_2BCC and BCCZ lattices. In the latter, having struts aligned with the loading direction, clear drops can be seen in the stress vs strain curve; furthermore, such drops decrease with increasing the relative density and consequently the strut thickness, coherently with what stated above. The same trends also characterized F_2BCC lattices despite the absence of struts along the building direction. Interestingly, in BCCZ lattices at very low relative density, the sudden drop reported by Gumruk et al. [77] happens right after the elastic region, suggesting elastic buckling since inelastic buckling is usually preceded by a deviation from the linearity as in [78]. The trends in the present work may agree with plastic buckling as the drops are preceded by a deviation from linearity. Nonetheless, given the dependencies observed with changing the relative density, other phenomena could play a role in this sudden drop in strength.

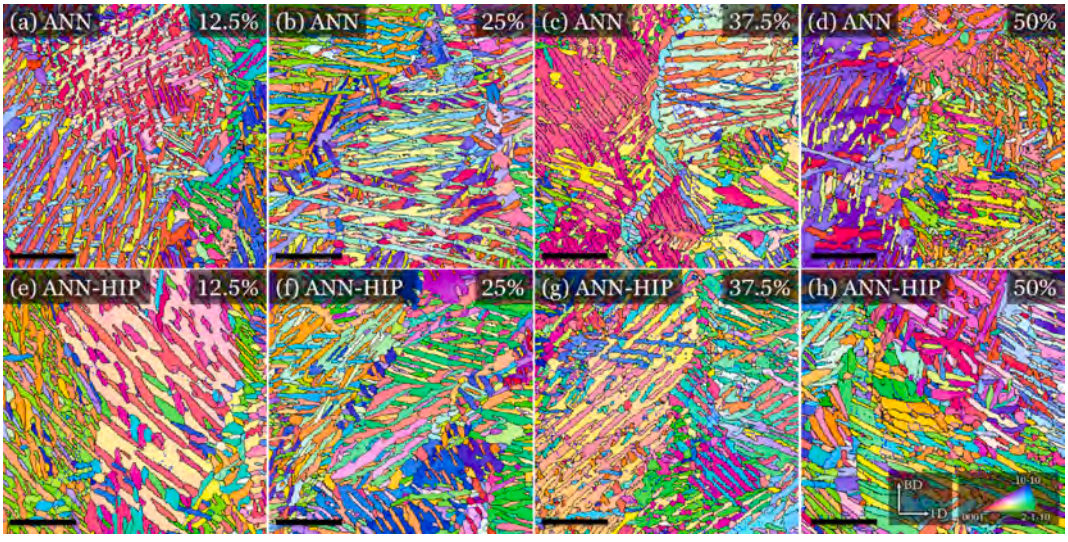

Fig. 3. BD-IPF maps of the specimens. (a–d) ANN conditions; (e–h) ANN-HIP conditions. Scale bar: 50 μm.

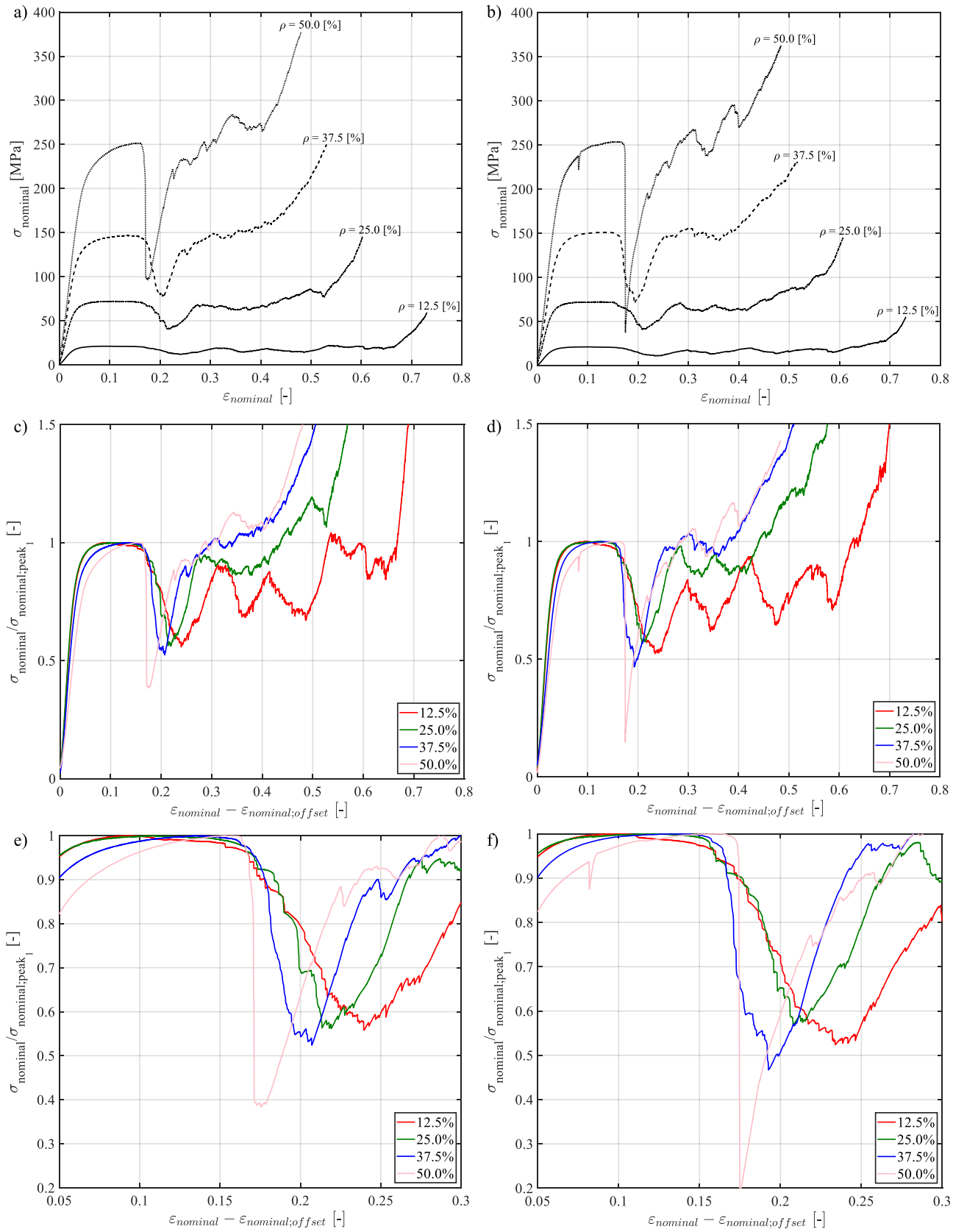

Fig. 4. Stress–strain curves under compression at different relative densities for (a) ANN and (b) ANN-HIP conditions (Note that some curves have been made available in [92] to illustrate the relative density effect on the lattice static behaviour). Nominal stress normalized by the first peak stress vs nominal strain (shifted by the offset strain) for (c) ANN and (d) ANN-HIP, with magnification of the first strength drop for (e) ANN and (f) ANN-HIP.

Let's consider a simple bending-dominated strut-based cell like a body-centred cubic (BCC) one, as in [74]. For a fixed cell size, the same global strain value results in the same displacement at the nodes. The deformed shape of a beam depends on constraints and loading conditions. Assuming a model similar to [74], rotations at the strut's end-sections and the deformed shape are the same regardless of the strut thickness. Under these assumptions, at the same global strain and cell size, being the deformed shape and its curvature the same, at a given section, larger struts would have higher maximum strains and stresses, being at higher distances from the neutral axis. Within the elastic regime, having assumed the curvature to be independent of the strut thickness, the stress would change with respect to the neutral axis according to the same law. In such a condition, plasticity happens in larger struts at lower global strains, considering that higher maximum stresses are reached. Adopting a simplified fracture criterion that would consider a maximum allowable value for strains, with higher thickness, such a value of strain triggering fracture is reached for lower values of the curvature, hence lower values of global strain. Conversely, thinner struts may experience plastic deformation and even contact with neighbouring struts before strains reach their allowable value to trigger fracture. In such a condition, struts would experience plasticity, but they would not experience fracture. Therefore, a plasticity vs fracture-dominated behaviour in the plateau region should depend only on the ratio between strut thickness and cell size (indirectly related to the slenderness of the struts) and on material ductility. Although such a model is handy to provide a general idea of some possible behaviour in the plateau region, it is affected by serious limitations, among which the fact that beam theory should not be applied if beams are not slender enough, especially when dealing with TPMS structures where ligaments have continuous variation in size.

A more plausible explanation for the observed trends in this work would involve both plasticity and fracture. As relative density decreases, higher global strains are required to reach the critical condition for the strength drop, and a larger fraction of the ligament cross-section can experience plasticity. Although plasticity is assumed to occur at all relative densities, at higher strut/wall thickness, conditions for fracture could be met before a substantial fraction of the section reaches plasticity; this results in a more brittle appearance. Moreover, as the relative density decreases, conditions for applying linear-elastic fracture mechanics should not be considered valid; an elastic–plastic fracture mechanism is more reasonable for the observed experimental results at lower relative densities assuming that extensive yielding occurs. Such a change in brittleness has also been documented by Choy et al. [79] who reported signs of ductile fracture with decreasing the relative density and hence the strut thickness. With a strut/wall thickness low enough, conditions for a plastic hinge could be achieved, resulting in a plateau not affected by fracture; such a condition can be found in the work of Maskery et al. [80]. In their work, a similar strength drop in aluminium alloy lattices has been observed when dealing with as-built conditions. In their case, heat treatments resulting in a significant increase in the strain at break [81] were identified as a solution to avoid such a drop in strength thanks to improved ductility. However, Maskery et al. [80] considered a strut/wall thickness significantly lower together with a slender strut with respect to other works involving titanium alloys that consistently report a plateau affected by severe fluctuations also for bending-dominated structures [20,71,72,82]. The influence of the strut/wall thickness and slenderness is also evident in the work of Bai et al [83]. Investigating BCC structures in a wider range of ratios between strut thickness and cell size, they demonstrated that a plateau without fluctuations in strength can be achieved with increasing slenderness. Further proof of the influence given by the ductility of the material on the fluctuations within the plateau region could be found in the work of Xiao et al. [84]; in their work, the drops in strength within the plateau region decrease with increasing test temperature, a trend that could be explained through the increased ductility with higher temperatures. In those cases that have buckling as the source of drops in strength, due to the fact that its critical conditions directly depend on the Young modulus, there could be a chance to have its effect even at elevated temperatures; an example can be found in the work of Wei et al. [85]. This also means that, if buckling is the source of the drop in strength within the plateau region, heat treatments aimed at improving the ductility may not provide significant changes. To further strengthen the considerations regarding the role of ductility, a comparison with the trends observed in some works investigating 316L lattice is useful [77,86–91]. In 316L lattices, regardless of the strut/wall thickness, the plateau regions, even in as-built conditions, show much smoother behaviour than those typical of titanium alloys. The difference can be linked to the higher elongation at break of 316L steel compared to Ti6Al4V.

The nominal stress–strain curves, shown in Fig. 4, allow for determining the quasi-static mechanical properties of these components according to ISO-13314:2011 [62]. An example of the analysis performed and the results for the entire experimental campaign are summarized in Fig. 5 (The results are also provided in Table S1).

One objective of this study is to investigate how the relative density affects the mechanical behaviour of solid-based gyroid lattices. In this regard, stiffness and yield strength of the lattice structures can be related to the relative density according to the Gibson-Ashby model [3,93]:

$$\frac{E}{E_{bulk}} = C_1 \cdot \left(\frac{\rho}{\rho_s}\right)^n$$

$$\frac{\sigma_{0.2}}{\sigma_{0.2,bulk}} = C_2 \cdot \left(\frac{\rho}{\rho_{bulk}}\right)^m$$

where E_{bulk} and $\sigma_{0.2,bulk}$ are the elastic modulus and yield strength of the bulk material, while C_i and n and m are constants dependent on the unit cell geometry [2,83].

Since experimental data for E_{bulk} and $\sigma_{0.2,bulk}$ were not available for both the conditions investigated, the Gibson-Ashby model was fitted by considering such unknowns into the constants C_i. In such a way the constants n and m were determined; their values are consistent with the theoretical ones for bending-dominated structures (with the theoretical values being 1.5 for the yield strength and 2 for the stiffness [2]).

Fig. 6 compares the yield strength results with data available in the literature. The difference in terms of yield strength with respect to specimens in AB conditions increases with increasing relative density. Moreover, specimens in AB conditions appear to follow a clear trend with changing the relative density, whereas the data for post-processed specimens exhibit a higher scatter. The collected data were fitted using Gibson-Ashby-like power laws, distinguishing according to the unit cell categories (TPMS vs strut-based lattices). The curves were obtained excluding the data for FFCm unit-cell geometry by Alana et al. [20] (marker: ×) and the solid-based gyroid by Mahmoud et al. [94] (marker: ◇), which clearly follow different behaviours. The possible reasons for these discrepancies are discussed in section 3.4. The fitting provided includes both bending and stretching-dominated unit-cells which are expected to follow different behaviours; the lack of sufficient data did not allow for distinguishing them in the present analysis. The fitted curves must be hence intended solely as indicative representations.

The numerical and experimental nominal stress–strain curves of the lattice structures in ANN conditions are shown in Fig. 7. The numerical results are presented for different fracture toughness values (K_c) of the bulk material. Good agreement is observed between the experimental and numerical compressive strengths (or peak stress) with a maximum deviation of about 5 % for the lattice with 50 % relative density, representing a first validation of the proposed FE model. The slight discrepancy in compressive strength can be attributed, among other factors, to the assumption of using the as-designed geometry, which can show some local geometrical deviations from the actual manufactured geometry (a comparison between experimental results and numerical

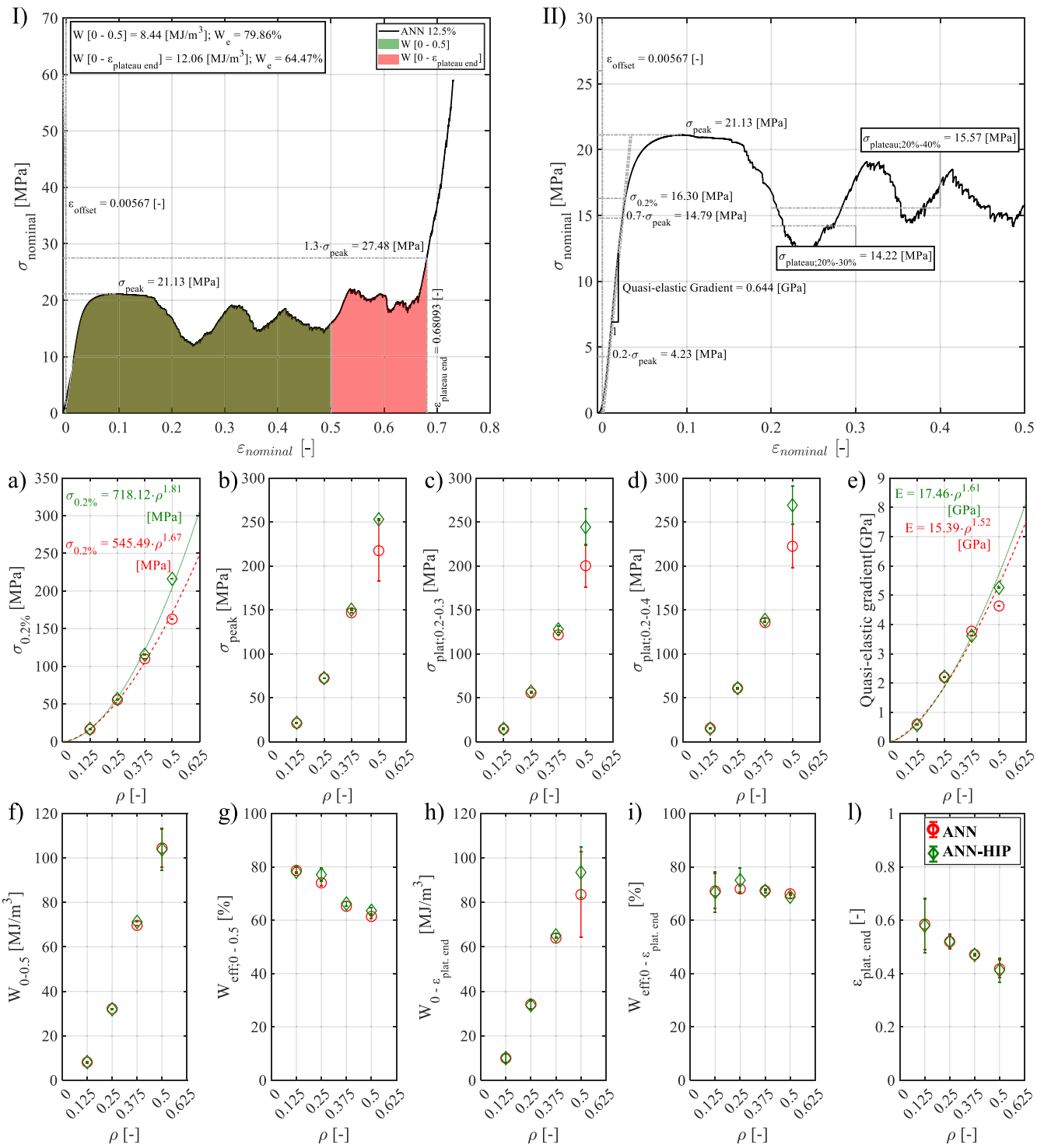

Fig. 5. (I) and (II): Quasi-static mechanical properties according to ISO-13314:2011[62]. Mean values with error bars for ANN (red) and ANN-HIP (green) conditions of: (a) yield stress (0.2 % offset) and Gibson-Ashby fitted curves; (b) first local stress peak; (c) plateau stress evaluated between 0.2 and 0.3 nominal strain;(d) plateau stress evaluated between 0.2 and 0.4 nominal strain; (e) quasi-elastic gradient and Gibson-Ashby fitted curves; (f) energy absorption up to 0.5 nominal straina; (g) energy absorption efficiency up to 0.5 nominal strain (defined as the ratio of the absorbed energy to the product of the strain range and the maximum compressive stress within the strain range); (h) energy absorption up to plateau end strain (defined as the strain at 1.3 the first peak stress); (i) energy absorption efficiency up to plateau end; (l) strain at the plateau end.

simulations performed on both the as-designed and micro-CT-reconstructed geometry is presented in Fig. S5). The compressive strength is independent of the selected fracture toughness value. The model overestimated the stiffness by about 60–80 % compared to the experimental data. This discrepancy likely arises from geometrical deviations between the designed and the as-built structures, and from neglecting surface and bulk defects in the FE model.

The stress fluctuations in the plateau region stem from the layer-wise collapse of the lattice structure (see Fig. 8) and they strongly depend on the fracture toughness of the bulk material. Crack propagation and damage evolution in the considered model are governed by the fracture toughness (K_c) and fracture energy (G_f) of the material, related in linear

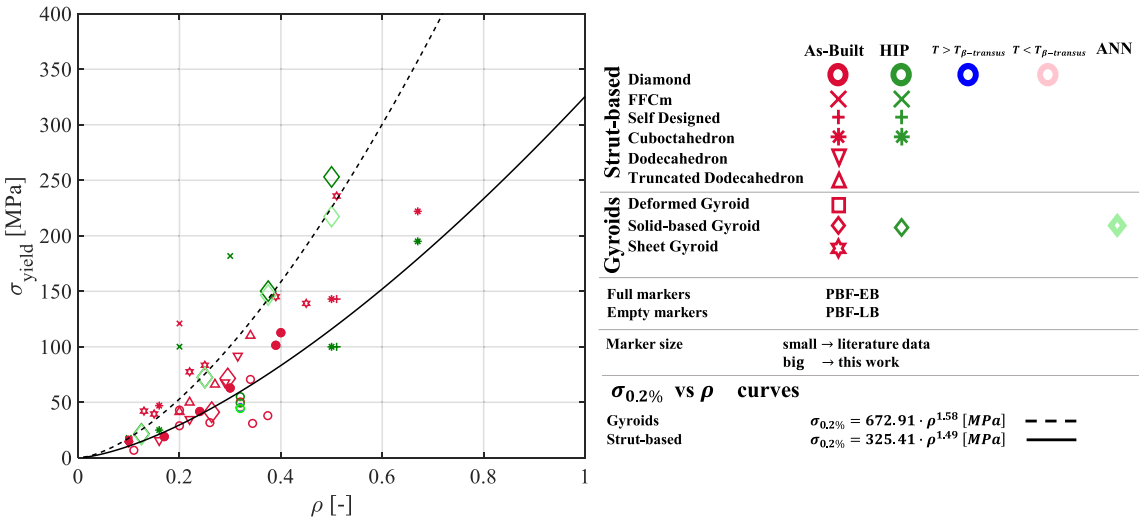

Fig. 6. Nominal yield strength vs as-design relative density including literature data [11,19,20,22,46,55,94–100] with Gibson-Ashby curves fitted for different unit-cell type (TPMS vs Strut-based). Due to the limited data and the high variability in parameters typical for AM, these curves must be intended as indicative representations.

elastic fracture mechanics as $G_f = \frac{K_c^2}{E'}$, where $E' = E$ for plane stress and $E' = \frac{E}{1-\nu^2}$ for plane strain conditions. Thus, G_f was calculated from K_c. Mode I plane strain fracture toughness value of about 50 $MPa\sqrt{m}$, reported for annealed PBF-LB Ti6Al4V [101] has been considered as a first estimation. This value led to a much more brittle plateau behavior than expected, as shown in Fig. 7(a) and(d). Increasing the fracture toughness reduced the amplitude of stress fluctuations and produced better agreement with the experimental behavior (see Fig. 7(a),(c) and(d)). Based on the first stress drop in the plateau region, fracture toughness values of about 75–85 $MPa\sqrt{m}$ best describes the deformation behavior of the lattices with 12.5 % and 25 % relative density, while the higher fracture toughness of about 85–95 $MPa\sqrt{m}$ better match higher relative densities (37.5 % and 50 %). The slightly lower fracture toughness at lower densities likely results from greater deviations in wall thicknesses (see Table 2). Subsequent stress fluctuations do not fully match the experimental results. The discrepancies between the fracture toughness values yielding the best numerical-experimental agreement and the literature value (50 $MPa\sqrt{m}$ in [101]) likely stem from the model's assumption of a linear-elastic fracture mechanism, whereas the observed experimental results suggest an elastic–plastic fracture mechanism. Applying limiting conditions derived from linear elastic fracture mechanics (LEFM) to an elastic–plastic fracture process can lead to apparently higher fracture toughness values. Ideally, a more accurate approach would involve a model incorporating elastic–plastic fracture mechanics (EPFM) and using limiting conditions derived from it. However, to the best of the authors' knowledge, models of this type −specifically tailored for lattices and capable of capturing both the linear-elastic response and the densification phase- are not yet available. Likewise, studies addressing elastic–plastic fracture behavior and providing the chance to evaluate the limiting condition for model calibration are currently lacking. Consequently, the fracture toughness value that yielded the best numerical-experimental agreement should not be regarded as a rigorous material property. Rather, it represents an apparent fracture toughness, serving as a practical parameter to compensate for the difference between the assumed (linear-elastic) and the actual (elastic–plastic) fracture mechanisms governing the plateau region. Furthermore, additional model simplifications may also contribute to the observed discrepancies. In particular, the assumption of a uniform fracture energy for all loading modes (I, II, and III), as well as neglecting anisotropy in damage initiation and propagation, could play a role.

3.4. Fatigue behaviour

Compression-compression fatigue tests were performed at a load ratio of 0.1 for the various relative densities and post-processing conditions considered. Fig. 9 reports the achieved results, showing the effect of the relative density in terms of nominal stress, as-designed effective stress and actual effective stress, while further analysed data are shown in Fig. 10. Finally, Figs. 11 and 12 present a comparison with literature data (complete database available in Tables S2−S5).

Relying on the statistical evaluation in Table 3, the highest difference between ANN and ANN-HIP specimens can be observed in the set having 12.5 % relative density, where ANN specimens slightly outperformed ANN-HIP ones at lower loads.

Grain size measurements and BD-IPF maps (see Section 3.2) achieved from metallographic analysis revealed a similar microstructure for both ANN and ANN-HIP components, explaining the overall negligible differences in fatigue behaviour across the post-treatment conditions analysed. However, this microstructural similarity alone could appear insufficient to justify the comparable fatigue performance observed. Typically, HIP treatment improvements in fatigue properties are usually expected due to both microstructural changes and reduced internal porosity. In this study, however, even the ANN specimens exhibited very low microporosity due to optimized process parameters; du Plessis et al. [50] also reported negligible microporosity for these process parameters. Additionally, the component geometry and loading conditions result in a stress state more critical at surface locations reducing the influence of internal microporosity.

Although the amount of β phase observed experimentally was limited, many studies report an $\alpha+\beta$ microstructure resulting from ANN and/or HIP treatments. Several works attribute the improvement in fatigue behaviour after HIP mainly to this microstructural change [46]. Typically, the α' martensitic phase of AB samples [37,98,102] transforms into the more ductile $\alpha+\beta$ phase although such a change is usually accompanied by grain coarsening [99,103]. Considering that low microporosity can already be achieved through optimized process parameters [50], other post-treatments may be regarded as competitive in the case of lattices. Hooreweder et al. [46], for instance, reported comparable fatigue performance for SR and HIP specimens; this result has been explained mainly with the change in microstructure from the α' martensitic phase of AB samples to the $\alpha+\beta$ phase for both SR and HIPed conditions. Hooreweder et al. [46] deemed as negligible the possible influence of residual stresses in lattices due to the struts' freedom to

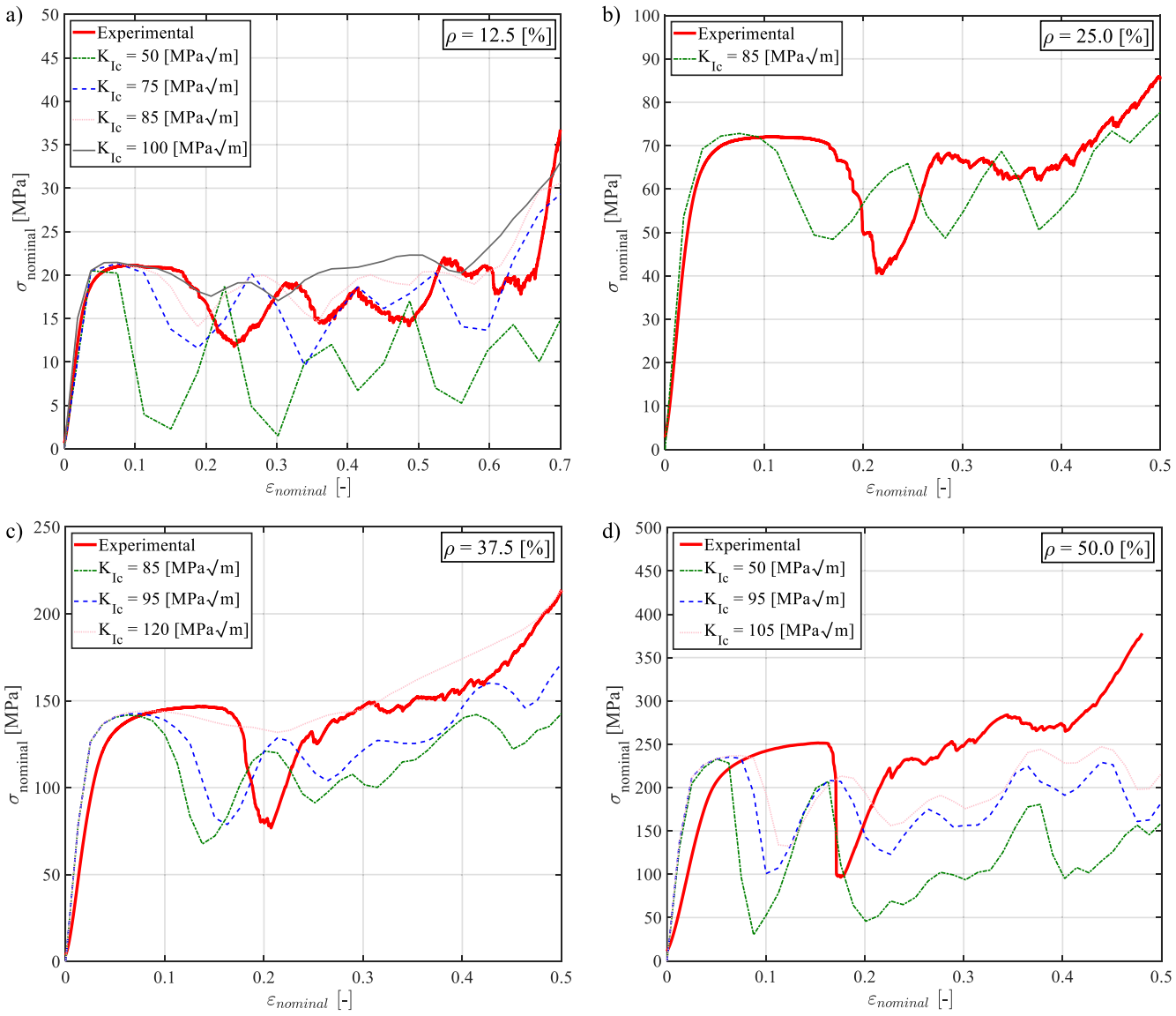

Fig. 7. Comparison of experimental and numerical nominal stress–strain curves for lattice in ANN condition with as-designed relative densities of (a) 12.5 % (b) 25 % (c) 37.5 % (d) 50 %. Legends values indicate fracture toughness. Numerical results are shifted along the strain axis by the experimental ε_{offset}.

deform. Nonetheless, literature presents some apparently contradictory findings regarding the residual stress effect in lattices. Ahmadi et al. [96], for example, investigated various heat treatments and found improved fatigue performance which was mainly attributed to a decrease in residual stress. Moreover, it is worth mentioning the work of Krijger et al. [22] that evaluated the effect of loading ratio on the compressive-compressive fatigue behaviour. Their fatigue data can be summarized in terms of stress amplitude with a relatively low scatter in the results; this is similar to the case of welded joints in which the effect of mean stress is disregarded due to high residual stresses [104]. Similar considerations can also be found in [29].

Relying on the dataset reported in Fig. 11 b, specific cases reveal significant improvements after HIP treatment as those in [20] (note the data at $\rho = 0.2$, marker: X) – however, these improvements are obtained with respect to an AB condition that did not undergo any heat-treatment hence not weakening the hypothesis that cheaper post-treatments can yield effects comparable to HIP-. Across the full dataset from the literature, the benefits of heat treatments appear marginal compared to those achievable by varying on the unit-cell type. In particular, strut-based and gyroids lattices, regardless of post-treatment conditions, clearly follow distinct trends and form separate data clusters. Interestingly, certain unit cell designs, such as the FFCm cell (marker: X) by Alana et al. [20], though strut-based, show fatigue performance within the cluster referable to gyroids. Conversely, the solid-based gyroid investigated by Mahmoud et al. [94] (marker: ◇) falls within the cluster referable to strut-based lattices. As discussed later in this section, these deviations could be attributed to notable differences in strut/ligament thickness compared to other samples of the same type, suggesting potentials for fatigue strength improvements by acting on this parameter.

Dealing with lattices tested in tensile conditions (Fig. 11(c) and(d)), HIP seems to induce a significant increase in fatigue properties compared to the as-built, no stress-relieved condition. Moreover, the collected literature data indicate that the influence of unit cell geometry – specifically strut-based vs. TPMS structures – under tensile loading differs from that observed under compression-compression conditions. However, these outcomes may be influenced by the testing conditions. The design of tensile test specimens still represents an open debate [2] with several issue related, but not limited, to: the specimen geometry – in [19,97] different solutions were considered-; the achievement of a proper stress state in the lattices zone; the need for solid regions for clamping with potential failure between the solid and the lattice part of

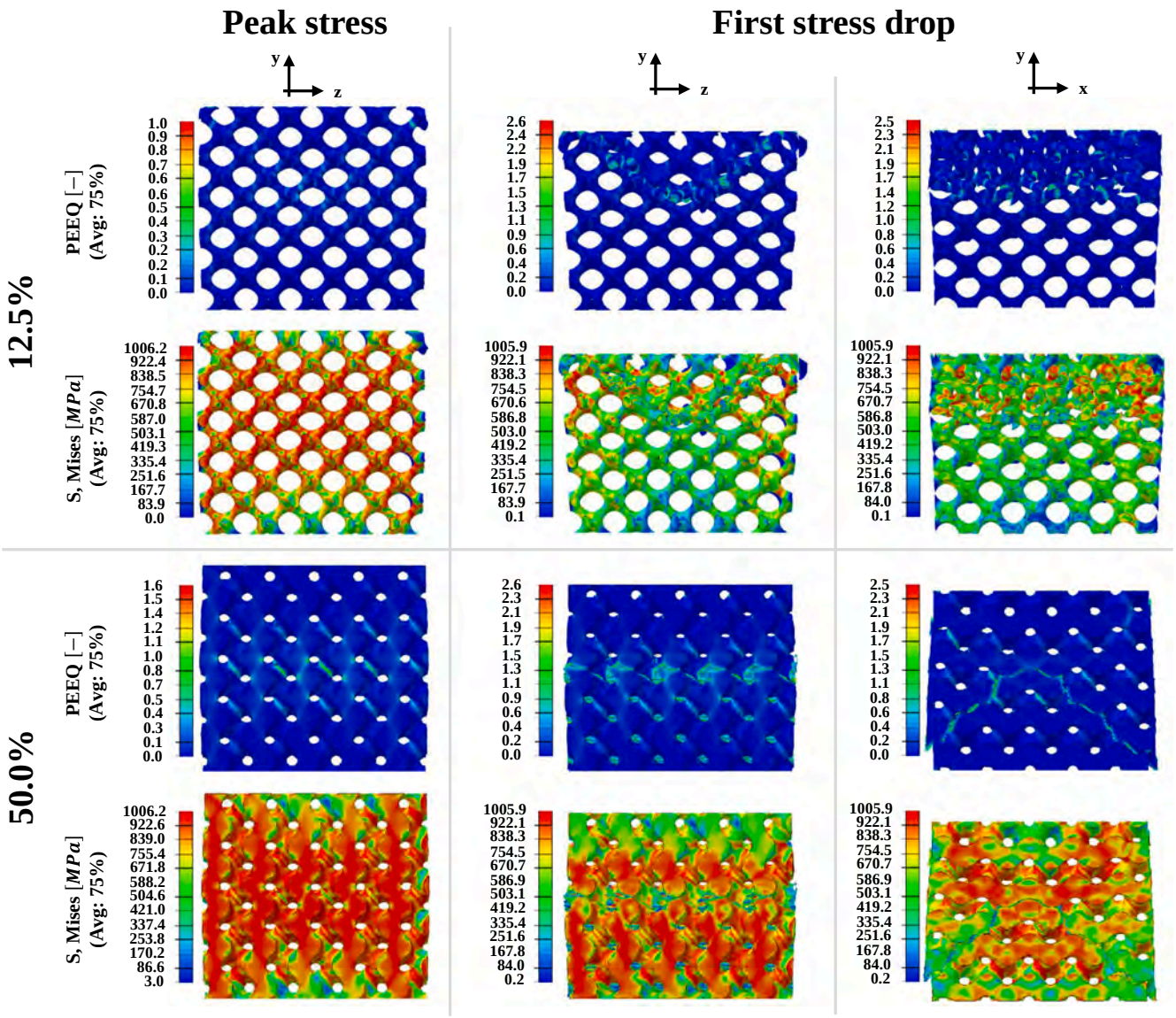

Fig. 8. Von-Mises stress and equivalent plastic strain (PEEQ) maps at the first peak stress and subsequent stress drop for lattices with 12.5% and 50% relative density, shown in two orthogonal views (XY and YZ), showing layer collapse.

the specimen; possible secondary bending effects due to distortion in the built specimens. In tensile tests, the normalized fatigue strength may help account for these influences on the fatigue response; as shown in Fig. 11 c-III and d-III, the improvement in fatigue properties due to HIP appear more limited when normalized.

Considering the two post-treatments analysed in this work, the slight differences noticed could be deemed as not significant, given the typical scatter in results of fatigue data. As shown in Table 3, the scatter in the results, for ANN and ANN-HIP together at equal design relative density, is quite low – at most 1.17 (P.S. 10 % and P.S. 90 %) – which is, of course, reflective of a larger amount of data but also of the limited difference between the two data sets. Therefore, the effect of relative density will be discussed considering the two sets of fatigue data together.

Considering the nominal stress values (Fig. 9I), which correspond to assuming the lattice structure as a metamaterial, the relative density effect on the overall mechanical behaviour is evident, having the specimens with $\rho = 12.5\%$ a fatigue strength as low as the 5 % of that at $\rho = 50\%$. A comparison with literature data, provided in Fig. 11 b-I, reveals that gyroids generally outperform strut-based unit cell lattices.

Evaluating the results using the as-designed effective stress value does not improve the correlation of fatigue data across different relative densities. Although the variation among relative densities is reduced (taking $\rho = 50\%$ as reference, the fatigue strength in terms of effective stress range decreases by ∼30 %, ∼ 56 % and ∼80 % for 37.5 %, 25 % and 12.5 % relative density, respectively) this approach does not yield a consistent correlation for the present unit cell design. Nonetheless, within a similar range of relative densities, Xu et al. [18] were able to significantly reduce the scatter in fatigue results for IN718 sheet-based gyroids. Conversely, referring to the broader literature fatigue dataset in Fig. 11 b-II, the effective stress still leaves a non-negligible dependence of the fatigue strength on the relative density, regardless of the unit cell geometry, manufacturing process, or post-treatment state. A similar situation is observed for lattices tested under tensile conditions in Fig. 11 d-II.

There is a need to have a methodology to account for the fatigue behaviour of lattices as relative density varies. Considering the results in Fig. 11 b-II and d-II, the use of effective stress alone should not be regarded as a valuable solution for this purpose. However, the effective stress can come in handy for evaluating how efficiently the bulk material properties are exploited. Dividing the nominal stress by the relative density means to account for the loss in strength attributable solely to the reduced amount of material. Practically, a constant effective stress

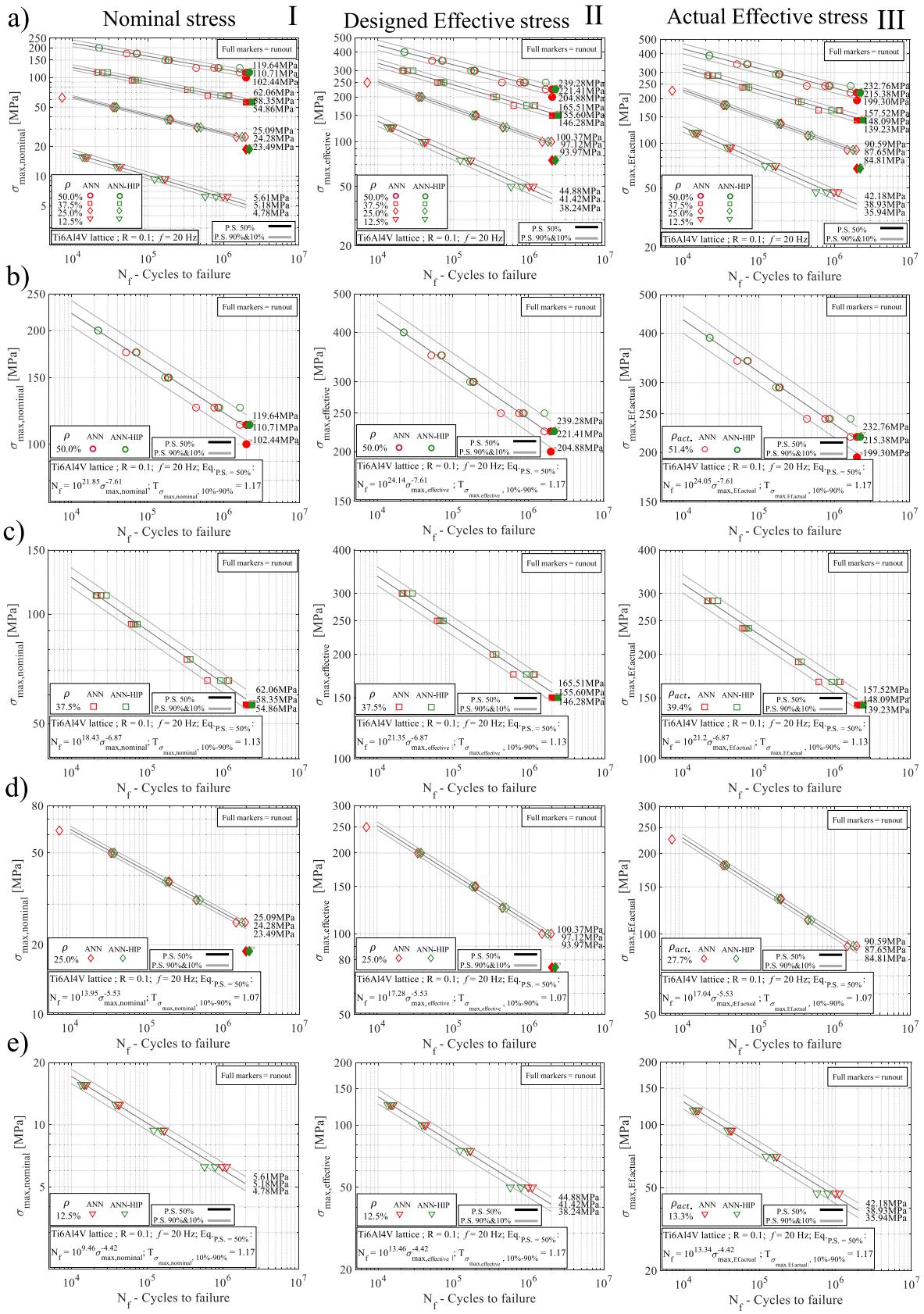

Fig. 9. (I) Maximum nominal stress vs number of cycles to failure (II) as-designed effective maximum stress vs number of cycles to failure and (III) actual effective maximum stress vs number of cycles to failure for: (a) all relative densities; (b) $\rho = 12.5\,\%$, (c) $\rho = 25\,\%$; (d) $\rho = 37.5\,\%$; (e)$\rho = 50\,\%$.

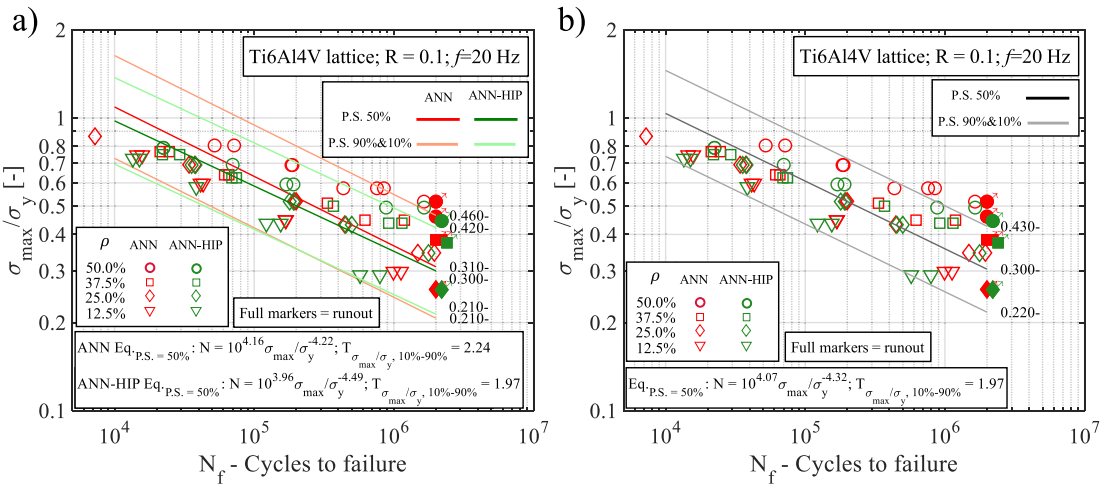

Fig. 10. Summary of fatigue test data showing normalized stress vs number of cycles to failure for: (a) ANN and ANN-HIP conditions analysed separately; (b) ANN and ANN-HIP conditions combined.

across different relative densities would indicate that the decrease in strength is fully explainable by the reduction in material. Conversely, a decrease in effective stress with decreasing the relative density – as observed in this work and in the literature data – implies that the bulk material mechanical properties capabilities are progressively less exploited. For example, if the purpose of a lattice component is a lightweight design, selecting lower relative densities may lead to the opposite outcome. Designing a simple component, such as the coupon specimens in this work, to sustain a given external load, the final design would result in a heavier lattice component with decreasing relative densities according to the observed trends. This conclusion holds true mainly for simple components such as the lattice specimens tested in this work; in real applications, lattices also enable tailoring metamaterials with mechanical properties that would not be achievable otherwise. Moreover, in real components, relative density can also be varied spatially according to the stress field due to the global geometry helping to reduce both stress concentrations and the overall weight of the designed part while maintaining a sufficient degree of safety.

An alternative approach to account for relative density is to use the normalized stress; it aims to indirectly account for effects of factors such as material, microstructure, relative density and deviation from the as-designed geometry [11]. The experimental data summarized using this approach are reported in Fig. 10 a) for ANN and ANN-HIP conditions and in Fig. 10(b) for the combined data sets; detailed values are provided in Table 3.

As observed, the data summarised according to the maximum stress normalized through the yield strength at different relative densities can be represented by a unique fatigue master curve having a scatter index of 1.97 (P.S. 10 % and P.S. 90 %) regardless of post-treatment conditions or relative densities of the specimens. Although the normalized stress provides a practical and easy-to-use solution for design purposes, Fig. 11 b-III indicates that fatigue strength in terms of normalized stress still appears to depend on relative density. Such an outcome can also be observed by comparing Fig. 11 b-I and Fig. 6 for gyroid lattices: nominal yield stress and the nominal fatigue strength vary according to different relationships – reported in these figures – with the relative density. Given the high variability in unit-cell design and process parameters across the data retrieved from literature, these curves should be intended only as indicative and aid for the present discussion. Nevertheless, the dependence of the ratio on relative density is clearly visible in Fig. 11 b-III. Furthermore, referring to Fig. 12, in the assumption that the normalized stress is able to account for the change in relative density of lattices, the fatigue strength (reported as maximum stress at 10^6 cycles) vs the yield strength would follow a linear relationship through the axis origin, with the normalized fatigue strength being the slope of this line. Although a linear relationship seems reasonable, the scatter in fatigue results in Fig. 11 a-III for the AB condition (red markers) suggests otherwise. Literature confirms that the accuracy of this approach varies among different works and depends also on the unit cell type considered [20–24]. Although the yield strength is often seen in literature as a valuable solution to account for the relative density effect, the fatigue properties are far more affected by surface roughness, unlike the quasi-static ones. This influence may be particularly significant for those lattices, such as TPMS, which feature continuous transition zones and are consequently more affected by surface roughness than strut-based lattices, where notch-like features are commonly localized at the strut junctions. This distinction can be clearly observed in Fig. 11 b-III referring to the various cell types reported.

In this regard, an influence can be observed on the inverse slope, *k*, of the fatigue curves in Table 3. *k* increases with the relative density resulting in a flatter fatigue response – an observation consistent with the findings of Xu et al. [18] for sheet-based IN718 gyroids. Referring again to the fatigue results in Fig. 11(b), two distinct fatigue behaviours can be identified for strut-based and gyroid lattices, neglecting a few exceptions (see results by [20], marked as ×, and by [94], marked as ◇). This difference can somehow be explained considering the main difference between these lattice types. Unlike strut-based structures, TPMS lattices feature continuous curved surfaces, ensuring the lack of nodes or curvature-discontinuity with a consequent reduction of stress concentrations. However, in the absence of sharp geometrical discontinuities, surface roughness assumes a more prominent role in the fatigue behaviour of TPMS structures. The dependency of the inverse slope, *k*, on relative density can be interpreted considering the ratio between surface roughness and ligament/wall thickness together with the trends of notched geometries [105]. Assuming that surface roughness parameters remain constant with varying the lattice relative density, increasing the relative density by acting on the ligament/wall thickness resembles a notch with a constant notch depth and an increasing ligament length. This leads to lower criticalities with increasing the relative density in lattice components by acting on the ligament/wall thickness. This interpretation aligns with the usual trends for notched components: keeping constant the load and simplifying the surface roughness as a notch having a constant depth (i.e., notch length), increasing the ligament length leads to lower gross stress concentration factors. In case yielding occurs, with the assumption of the surface roughness as micro notches, possible changes in the inverse slope of the SN curve would be expected; this appears consistent with the steeper curves observed at lower relative density in this study. The extent of this variation depends

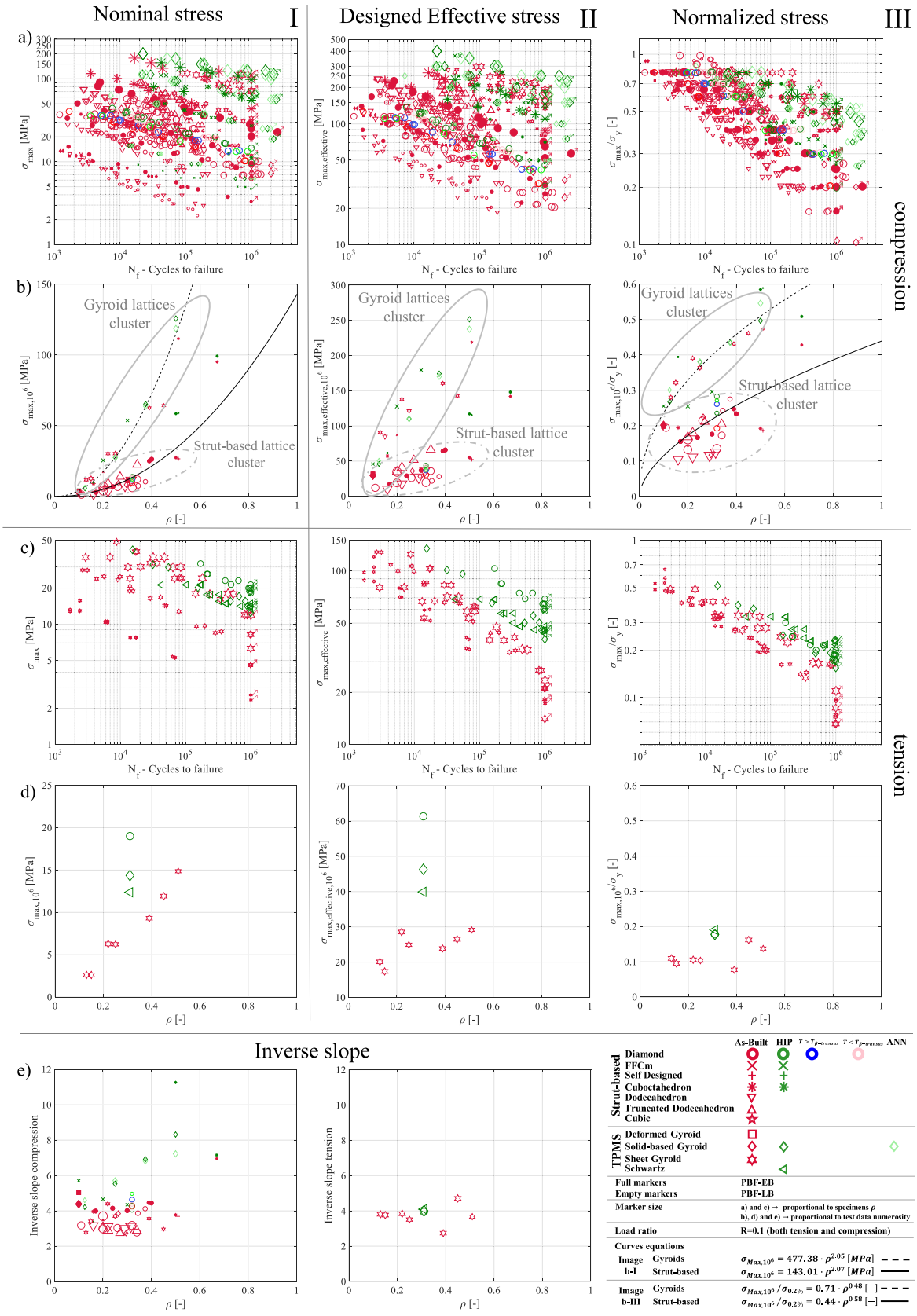

Fig. 11. Summary of Ti6Al4V fatigue data from this work and literature [11,19,20,22,46,55,94–100] at a load ratio of 0.1 (both in tension and compression) presented using: (I) nominal stress; (II) effective stress and (III) normalized stress. For each approach it is reported: (a) & (c) stress vs number of cycle to failure; (b) & (d) fatigue strength at 10^6 cycles vs relative density. (e) Inverse slope of the fatigue curves vs relative density derived by interpolating Basquin-like equations (Notes: since effective and normalized stresses are derived from the nominal one through a multiplying factor, the inverse slopes coincide in the various approaches; Due to limited data and high variability in parameters typical of AM, the Gibson-Ashby fitted curves must be intended as indicative representations).

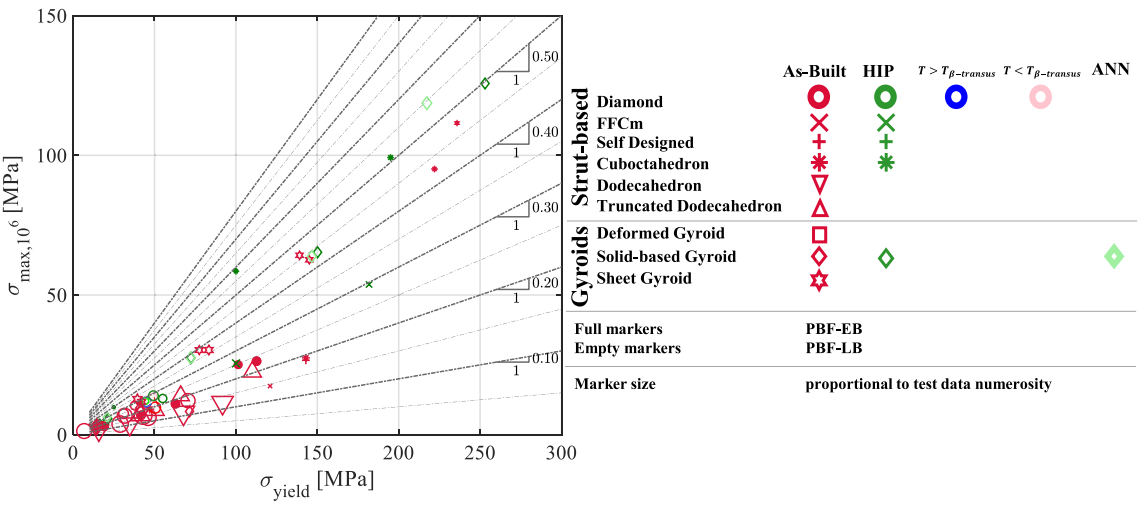

Fig. 12. Maximum nominal stress at 10^6 cycles vs yield strength. Data from literature [11,19,20,22,46,55,94–100].

Table 3
Fatigue properties for the different relative densities and post-processing conditions according to effective and normalized stress.

Approach	ρ	Post-processing conditions	P.S. 90 % [*MPa*]	P.S. 50 % [*MPa*]	P.S. 10 % [*MPa*]	*Scatterindex* [−]	k [−]	C $\left[\frac{Cycles}{MPa^{-k}}\right]$	%*
$\sigma_{max,effective} = Load/(\rho \bullet Section)$	12.5 %	ANN	42.44	43.72	45.04	1.06	4.65	$10^{13.92}$	−80
		ANN-HIP	35.20	39.04	43.30	1.23	4.21	$10^{13.01}$	−83
		Both sets	38.24	41.42	44.88	1.17	4.42	$10^{13.46}$	−81
	25 %	ANN	91.01	97.08	103.57	1.14	5.52	$10^{17.27}$	−55
		ANN-HIP	94.29	97.16	100.12	1.06	5.53	$10^{17.30}$	−58
		Both sets	93.97	97.12	100.37	1.07	5.53	$10^{17.28}$	−56
	37.5 %	ANN	138.45	153.65	170.52	1.23	6.81	$10^{21.20}$	−29
		ANN-HIP	147.06	157.54	168.76	1.15	6.92	$10^{21.51}$	−32
		Both sets	146.28	155.60	165.51	1.13	6.87	$10^{21.35}$	−30
	50 %	ANN	197.28	215.67	235.77	1.20	7.23	$10^{23.16}$	Ref**
		ANN-HIP	209.47	231.35	255.51	1.22	8.32	$10^{25.97}$	Ref**
		Both sets	204.88	221.41	239.28	1.17	7.61	$10^{24.14}$	Ref**
$\sigma_{max,actualeffective} = Load/(\rho_{actual} \bullet Section)$	13.3 %	ANN	39.89	41.09	42.33	1.06	4.65	$10^{13.80}$	−80
		ANN-HIP	33.08	36.69	40.69	1.23	4.21	$10^{12.89}$	−84
		Both sets	35.94	38.93	42.18	1.17	4.42	$10^{13.34}$	−82
	27.7 %	ANN	82.14	87.62	93.47	1.14	5.52	$10^{17.02}$	−58
		ANN-HIP	85.1	87.69	90.36	1.06	5.53	$10^{17.05}$	−61
		Both sets	84.81	87.65	84.81	1.07	5.53	$10^{17.04}$	−59
	39.4 %	ANN	131.78	146.24	162.3	1.23	6.81	$10^{21.05}$	−30
		ANN-HIP	139.97	149.94	160.62	1.15	6.92	$10^{21.36}$	−33
		Both sets	139.23	148.09	157.52	1.13	6.87	$10^{21.20}$	−31
	51.4 %	ANN	191.91	209.80	229.35	1.20	7.23	$10^{23.08}$	Ref**
		ANN-HIP	203.77	225.05	248.55	1.22	8.32	$10^{25.87}$	Ref**
		Both sets	199.30	215.38	232.76	1.17	7.61	$10^{24.05}$	Ref**
			[−]	[−]	[−]	[−]	[−]	[*Cycles*]	
$\sigma_{max,nom}/\sigma_y$	All	ANN	0.21	0.31	0.46	2.24	4.22	$10^{4.16}$	
		ANN-HIP	0.21	0.30	0.42	1.97	4.49	$10^{3.96}$	
		Both sets	0.22	0.30	0.43	1.97	4.32	$10^{4.07}$	

* Reduction in fatigue strength at 2×10^6 compared to the **reference case (Ref).

on the yielding of material around the notch head. In such cases, plastic deformation can cause a larger difference between the fatigue notch factor and the elastic stress concentration factor. This means that, in case of yielding, the extent of fatigue strength variation as a function of roughness to thickness ratio can be lower than expected.

While this explanation provides a sound rationale for the results obtained in this study and in Xu et al. [18] for IN718 sheet-based gyroids, the results reported by Kelly et al. [19] (see sheet-based gyroids in Fig. 11 e-I and e-II) appear to weaken this interpretation. However, the results in [19] were tested in AB conditions, unlike those in the present work. In AB conditions, it would be reasonable to expect higher notch sensitivity leading to a lower dependency of the inverse slope on the roughness/thickness ratio and, indirectly, on relative density. Moreover, since the specimens in [19] were in AB condition and not stress-relieved, residual stresses may have influenced the differences with the results in the present work.

Higher inverse slopes after heat-treatment or HIP are also exhibited by some strut-based unit cells. These results, together with the results of Hooreweder et al. [46], who investigated the effect of chemical etching on the fatigue behaviour of diamond unit-cell lattice, suggest that the explanations discussed above may also be extended to this kind of unit cells. Nonetheless, due to the limited data available at different relative densities (see green, blue and pink diamond markers in Fig. 11 e-I compared with the red ones) and the relatively small difference in inverse slope, general conclusions cannot yet be drawn. Because strut-based lattices are characterized by severe notches at the node intersections, surface roughness should not be expected to have as strong an effect as in TPMS. Indeed, in the results by Ahmadi et al. [96], negligible effects on the fatigue behaviour can be observed after surface treatments such as sandblasting and chemical etching; this could be interpreted as evidence of the dominant influence of severe notches at the node intersection on strut-based lattices. Some literature results in literature – such as those of Wu et al. [100] (Cuboctahedron in Fig. 11, marker: ✱) or of Alana et al. [20] (marker: ×) – show trends that do not agree with the explanation above. Comparing the unit cell geometry studied in [20] and the one in [100], a possible explanation can be obtained: although the cell sizes in these two works are almost the same, the design adopted by Alana et al. [20], with fewer struts per cell, resulted in significantly thicker struts than those in [100]. A similar consideration applies to the results of Mahmoud et al. [94], whose solid-based gyroids, at the chosen relative density and cell size, had ligament thickness of 200μm and 400μm, substantially smaller than those in the present study. Consequently, at the same relative density, the strut/ligament thicknesses of the lattices among [94] and this work are not directly comparable which may partly explain the apparent different trends found in [94]. Although A quantitative analysis was not performed by the authors due to lack of appropriate data, the consistency in trends across other literature data may also be attributed to similar strut thicknesses between different unit cell type at comparable relative densities. Therefore, the investigation of the fatigue behaviour of those lattice cells would still be incomplete having overlooked the possible combinations of parameters leading to the same relative density.

From the above discussion, it becomes clear that interpreting the fatigue behaviour of lattice components solely in terms of relative density and unit cell type limits the observation to the single tiles of a much more complex mosaic. By doing so, apparently contradictory outcomes or outlier results easily arise from the literature (see results by Wu et al. [100] and Alana et al. [20] as an example) despite suitable explanations can be found by just widening the set of parameters involved. Alongside the relative density and the unit cell geometry, the strut thickness, surface roughness and microstructure cannot be overlooked to fully understand and foresee the fatigue behaviour of lattice components and hence exploit their capabilities.

The literature data retrieved and analysed in this work did not provide the level of detail required to explore the applicability of local approaches, which have the potential to overcome some of the limitations inherent to global approaches. Nevertheless, local approaches, relying on a unique fatigue curve, do not allow for a direct evaluation of the design quality. For instance, assuming local approaches capable of fully predicting the fatigue behaviour of lattice structures, the fatigue data analysed in this work would collapse onto a single fatigue curve dependent solely on the post-treatment condition. Consequently, the considerations done regarding the bulk material properties exploitation could not have been directly evaluated. Ideally, the two methodologies should be integrated: local approaches could be employed to assess fatigue behaviour based on the bulk material properties, while global approaches – such as the effective stress – could be used to rank and compare different lattice designs. However, local approaches may also present intrinsic limitations. They were originally derived and formalized for conventionally manufactured components whose dimensions are significantly larger than microstructural features. Experimental evidence on conventionally manufactured materials has shown that, depending on the ratio between component dimensions and microstructural features, the material may exhibit distinct fatigue behaviours. Consequently, lattice structures – characterized by a low ratio between geometrical and microstructural features- may behave differently from larger-scale components on which local approaches have been extensively validated, potentially limiting the applicability of such approaches to lattices [2]. Therefore, although the use of local approaches for lattice components remains promising, they may still fail to account for all the relevant influencing factors within a unifying fatigue design approach.

3.5. Fatigue failure assessment

The tested specimens were investigated using SEM analysis. Different failure mechanisms were expected depending on both the relative density and the post-treatment conditions.

As regards the post-treatments, several aspects deserve consideration; in general, possible signs of their influence on the fatigue behaviour must be expected due to both microstructural and internal porosity changes. As reported by Yu et al. [106], post-processing treatments can improve fatigue performance by increasing the threshold for crack growth and improving the fatigue crack growth properties. Additionally, the reduction in internal porosity achievable through HIP treatment could decrease the number of potential fatigue crack initiation sites, thereby improving the fatigue performance. Based on these observations, beneficial effects should be expected for both specimen sets; in ANN specimens, they should be mainly attributed to microstructural changes, while in the HIPed ones, a synergistic action of both microstructural change and internal porosity reduction is likely. Notably, working on HIPed specimens, Yu et al. [106] reported improvements dominated by the variation in internal porosity, while Alana et al. [20] observed influences dominated by the microstructural change.

Concerning possible beneficial effects arising from a change in the microporosity, the process parameters used in this work have been thoroughly analysed by du Plessis et al. [50]. For the same scan speed, hatch spacing, hatch strategy, and layer thickness, they observed negligible microporosity in stress-relieved specimens realized with laser power values between 200 W and 300 W. Therefore, the process parameters used in the present work are expected to yield very low microporosity even in the as-built conditions; consequently, the additional benefits of HIP treatment due to reducing the microporosity may only act to a limited extent. Thus, any remaining differences in fatigue behaviour between ANN and ANN-HIPed specimens must originate from microstructural variations. However, as shown in section 3.2, the microstructures of ANN and HIP specimens are comparable in terms of grain size, phase constitution, and directionality. This similarity, combined with the absence of noticeable differences in microporosity, explains the lack of significant variation in fatigue performance observed experimentally when the relative density is held constant. This strengthens the consideration that, in lattices, the combination of optimized process parameters, yielding minimal microporosity, with post-treatments that lead to a similar microstructure is already sufficient to achieve beneficial effects equivalent to those of HIP treatment.

The conducted analysis provides valuable insights into the locations and mechanisms of crack initiation leading to failure. As shown in Fig. 13, which reports SEM images acquired on interrupted fatigue tests, fatigue crack initiation usually occurred in the higher stressed regions, specifically at micro-notches formed by the characteristic surface roughness of the AM component. The influence of these micro-notches is further confirmed by the presence of multiple cracks initiating within the same highly stressed region (see the magnified image of the 37.5 % relative density specimen in Fig. 13). These cracks propagated vertically and originated from several locations, on both the upskin and downskin surfaces. Eventually, they led the entire specimens to fail in a diagonal shear pattern.

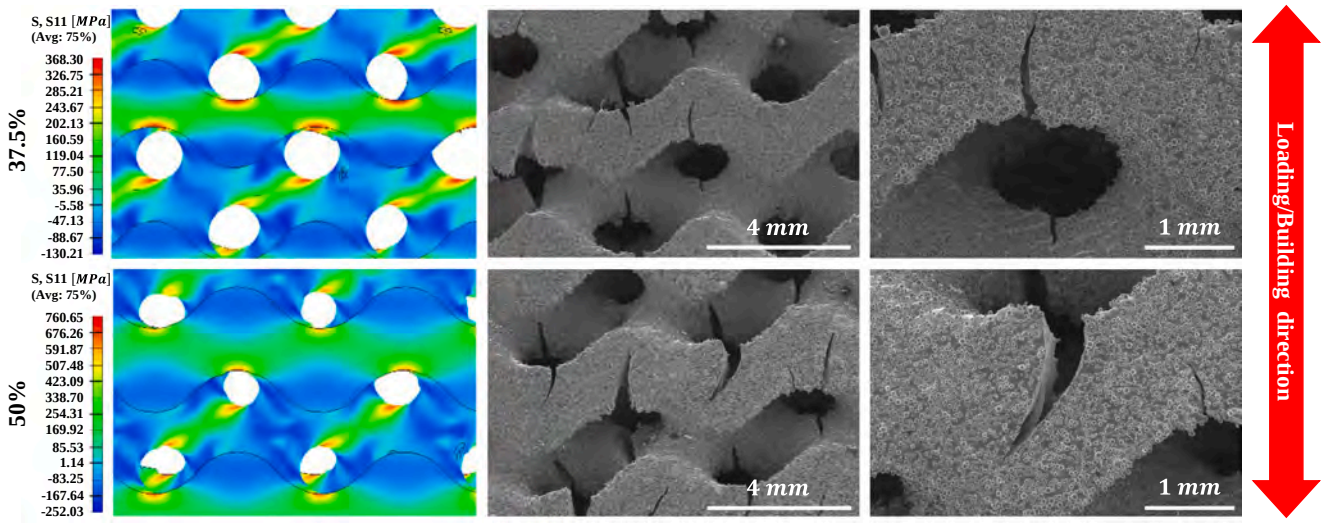

Fig. 13. SEM images of global fracture patterns from interrupted tests showing fatigue crack initiation sites and their correlation with numerical stress analysis.

The complex geometry of lattice structures induces stress gradients, with higher stresses at the outer surfaces, making relevant not only the size, but also the location of pores. A pore large enough to potentially trigger fatigue failure was revealed by the post-mortem analysis; however, as shown in Figure S 6, the fatigue crack initiated at the outer surface. Therefore, even in the presence of non-negligible microporosity, its location in a lower-stressed region reduces the possible detrimental effect on the fatigue behaviour.

Considering the discussions above, sub-surface defects could be of particular interest since, if not open to the free surface, they are usually

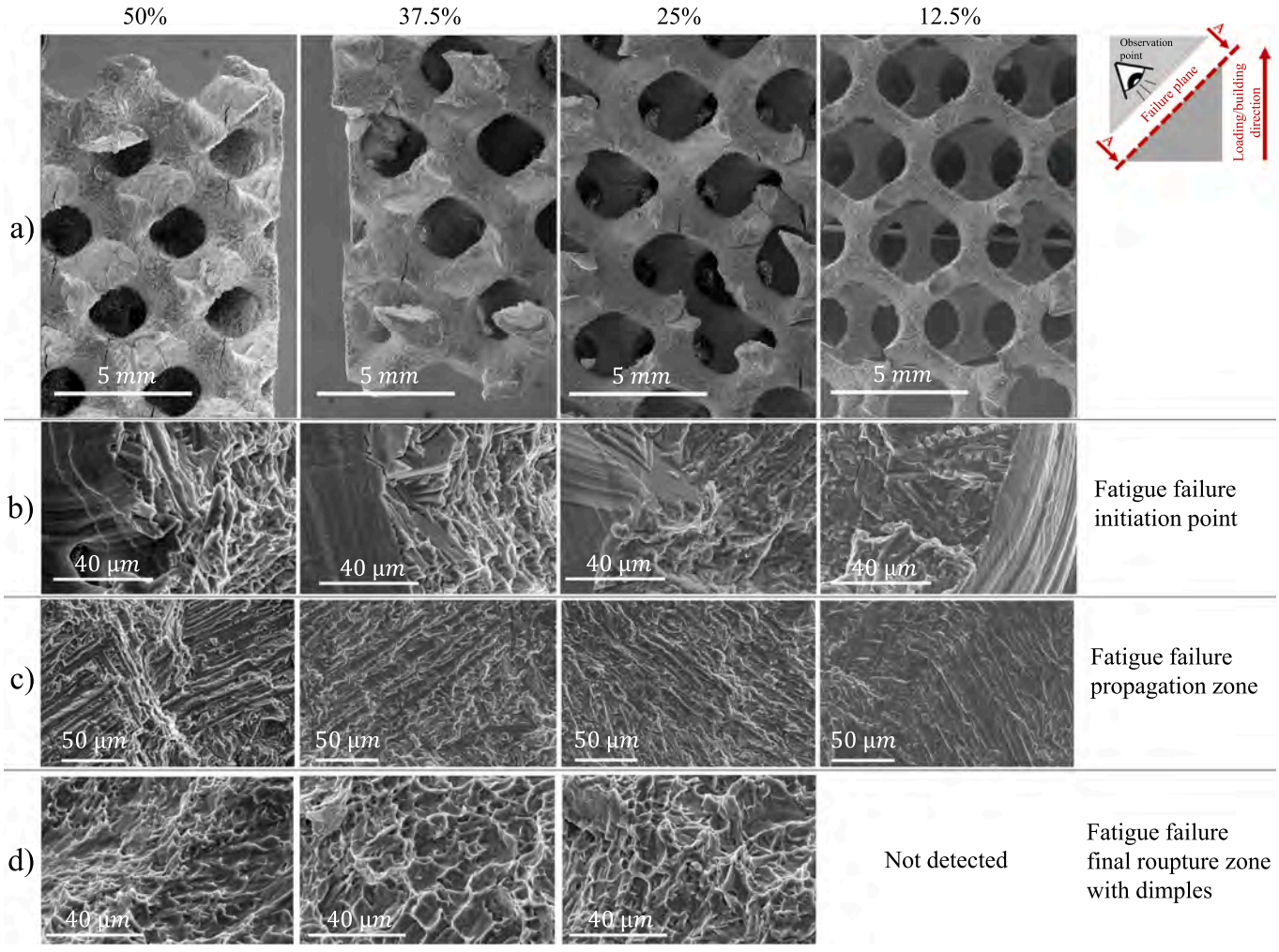

Fig. 14. Fatigue fracture analysis showing the final condition of the investigated specimens after reaching 20 % of global strain.

reduced in size by HIP treatment [107]. To assess their possible influence, failure initiation zones were carefully examined to determine whether such defects were present at the crack initiation sites.

Through SEM analysis, in all cases investigated, crack initiation was identified by the microstructural features on the fracture surface; no evidence of subsurface defects was observed. The crack initiation features were consistent across all relative densities, as shown in Fig. 14(b). The first stage of the crack growth, highlighted in Fig. 15(b), appears to strongly depend on the microstructural features following the grain morphology in this region. At longer crack lengths, the crack grew with a combination of intergranular and transgranular features producing a tortuous fracture surface with a basketweave-like texture, particularly evident in the propagation zone as reported in Fig. 14(c) and Fig. 15(c).

Fig. 14(d) reports the final stage of the fatigue failure. In this zone, the fracture surface appears highly tortuous, showing ductile static failure features such as dimples with micro-void coalescence. Due to the thin ligaments, this zone likely involves a competition between plastic collapse and ductile tearing. The fatigue failure surfaces also align with the outcomes reported by Razavi et al. [105] while investigating the thickness effect. In [105], three different zones for the fatigue failure were identified, i.e., an initial stable crack growth followed by a quasi-stable and a final unstable one. In their study, the stable crack-growth region decreased with the specimen thickness decreasing; given the much smaller thickness in our work, the extent of this zone is considerably reduced, resulting in a fracture surface mainly divided into a quasi-stable crack growth zone and an unstable one.

As shown in Fig. 13, the fatigue failure in lattices is characterized by several cracks, of generally different lengths, growing at different locations; this usually leads to strut failures at different numbers of cycles. The failure of each strut redistributes the load among the still unbroken struts, altering their local loading conditions. Therefore, considering only the initial loading state could be misleading. This load redistribution can change the crack-opening mode in the unbroken ligaments, possibly introducing mixed-mode fracture features [108]. For instance, early-failed struts experience lower loads than the last ones to fail, resulting in differences in the extent of the fracture surface zones discussed above. Under these considerations, the unstable crack-growth zone tends to show a different extent between early-failed (lower load) and late-failed (higher load) struts; in some cases, we did not observe a clear zone with the presence of dimples as with the 12.5 % relative density specimen in Fig. 14(d). This, however, does not imply that such zones cannot be found in other failed struts at the same relative density. Fig. 16 further illustrates the failure surfaces of two ligaments at 25 % and 12.5 % relative densities, showing different appearances at the final stage of failure (Fig. 16 (g) and (h)(), including possible signs of surface contacts.

4. Conclusions

In this work, a comprehensive experimental campaign was conducted to investigate the quasi-static and fatigue behavior of Ti6Al4V solid-based gyroid lattices, made via PBF-LB. The study specifically investigates the influence of relative density (four different values) and post-treatment conditions (stress relieving and annealing, ANN, and stress-relieved, annealing and hot isostatic pressing, ANN-HIP). While the experiments directly focused on these two factors, the study aims to interpret their effects in a wider perspective and examine a possible process optimization framework for lattices, exploring whether cheaper and less complex post-treatments than HIP could match its beneficial effects. The experimental campaign was complemented by micro-CT scans, microstructural and postmortem analysis for understanding damage mechanisms and FE modelling to evaluate the stress distribution and correlate experimental findings. The obtained results were compared with literature data, seeking a more comprehensive analysis. The main outcomes of the investigation can be summarized as follow:

- Micro-CT analysis revealed 10 % higher actual relative density and 14 % lower wall thickness than their as designed values. These contradictory outcomes originate from significant deviations at the specimens' outer surfaces indicating that average relative density may not accurately represent the core one.
- No significant differences were observed in texture, grain size, or residual strain, either at the edge or in the central part of the ligaments analyzed across all conditions. EBSD analysis consistently identified only the α-Ti phase.
- The comparison between ANN and ANN-HIP specimens revealed a comparable mechanical behavior, proving that the combination of optimal process parameters and cheaper post-treatments can match the benefits due to HIP.
- The nominal fatigue strength decreased substantially with decreasing the relative density (∼ 47 %, ∼ 78 %, and ∼95 % lower

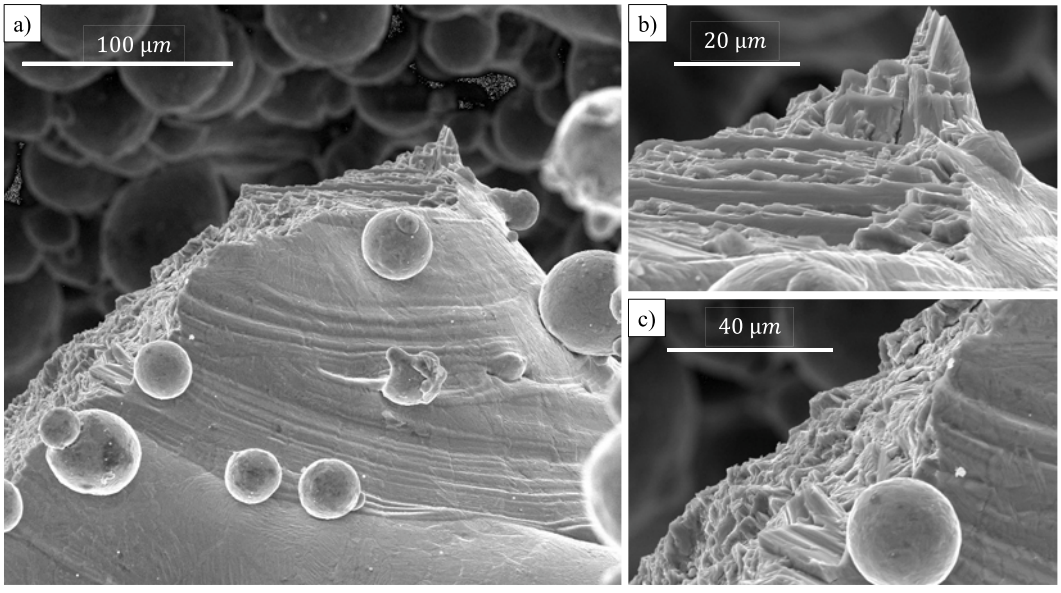

Fig. 15. (a) Side view of a fracture surface in a specimen with a 12.5 % relative density showing, (b) fracture along the microstructures and (c) intergranular-transgranular appearance.

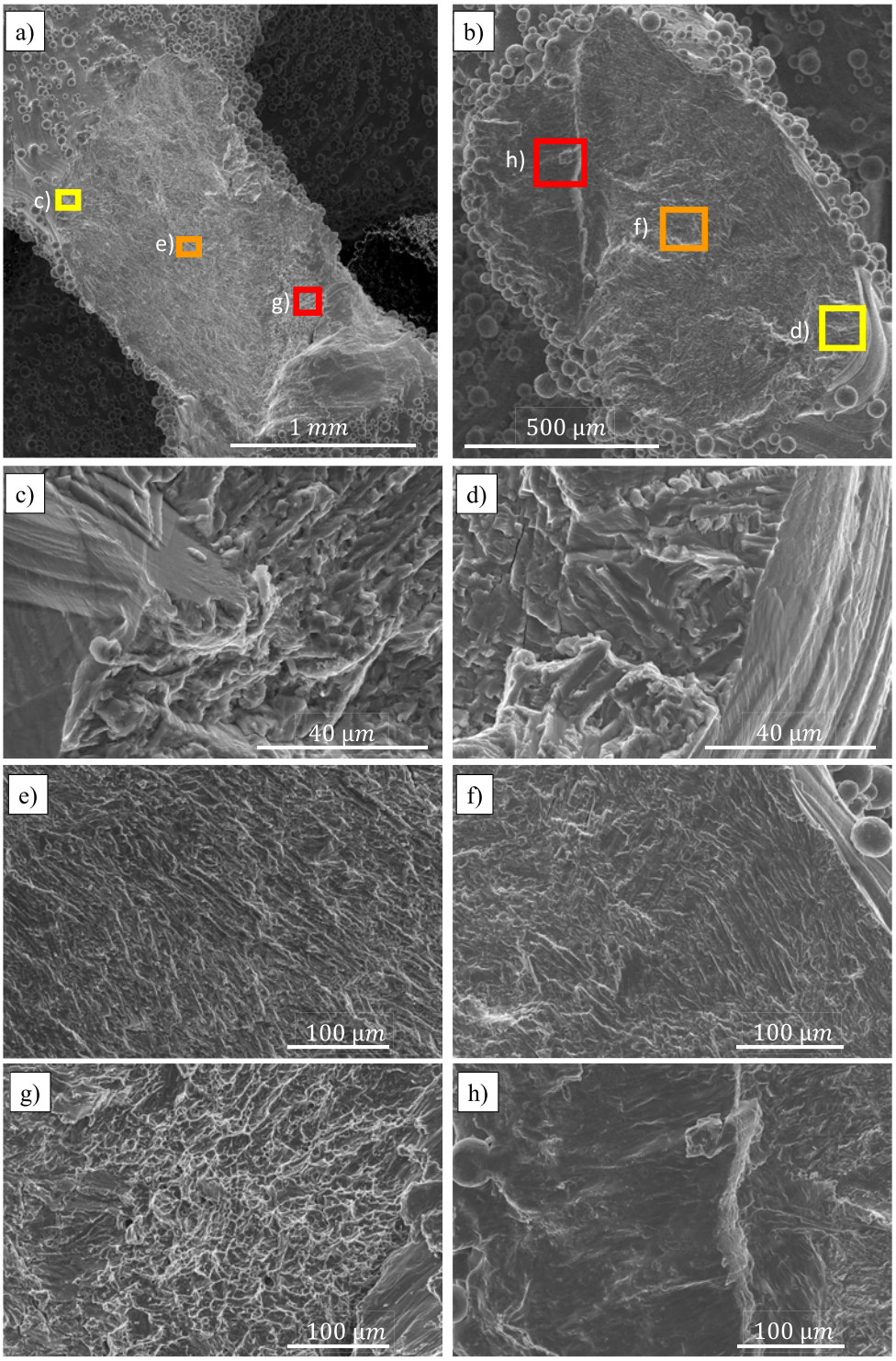

Fig. 16. Failure surface of a single strut at (a) 25 % and (b) 12.5 % relative density; (c) and (d) are the crack initiation sites for 25% and 12.5%, respectively; (e) and (f) are the crack propagation zones for 25 % and 12.5 % respectively; (g) and (h) are the final crack growth zones showing dimples for 25 % and possible contact between surfaces for 12.5 %.

for 37.5 %, 25 %, and 12.5 % relative density, respectively, compared to the 50 % one at 2 million cycles).

– The effective stress failed to relate fatigue strength to relative density. Nevertheless, this parameter is useful to evaluate the efficiency in exploiting the bulk material properties as it accounts for loss in strength due solely to material reduction. The analysed data revealed that the efficiency in exploiting the bulk material decreases with decreasing the relative density; paradoxically, lower relative densities lead to heavier designs for a given load-bearing requirement.
– The normalized stress provided a reasonable correlation of fatigue strength values across relative densities, though it is affected by a residual dependency likely attributable to the different influence of the surface roughness on quasi-static and fatigue behaviour. This interpretation is supported by the higher residual dependency

observed in gyroid lattices, whose continuous transition zones make surface roughness dominant on the fatigue behaviour. Conversely, in strut-based lattices, the sharper notches at strut nodes compete with the surface roughness, thereby reducing its influence. Basquin-like equation slopes further corroborated this interpretation.
– FEA, performed on as-designed geometry, captured the key aspects of lattice quasi-static behavior, with minor discrepancies in stiffness data. It also confirmed the marginal role on the quasi-static behavior of surface roughness that, however, cannot be neglected considering the fatigue behavior.
– Finally, the failure analysis showed fatigue cracks initiated at the surface, strongly influenced by surface roughness but coherent with the critical zones identified by FEA. This also implies that internal microporosity, located in lower-stressed zones, has a reduced impact on the fatigue behavior and is tolerable to a limited extent. Proofs of this have been provided by the failure analysis.

Funding sources

This research did not receive any specific grant from funding agencies in the public, commercial, or not-for-profit sectors.

CRediT authorship contribution statement

Pietro Foti: Writing – original draft, Visualization, Methodology, Formal analysis, Data curation, Conceptualization. **Asghar Heydari Astaraee:** Writing – review & editing, Investigation, Formal analysis. **Sara Bagherifard:** Writing – review & editing, Validation, Resources, Methodology, Conceptualization. **Anton du Plessis:** . **Di Wan:** Writing – review & editing, Investigation. **Filippo Berto:** Writing – review & editing, Resources, Methodology. **Nima Razavi:** Writing – review & editing, Validation, Supervision, Resources, Project administration, Methodology, Investigation, Conceptualization.

Declaration of competing interest

The authors declare that they have no known competing financial interests or personal relationships that could have appeared to influence the work reported in this paper.

Acknowledgements

The authors would like to thank Quintus Technologies for their assistance in performing the Hot Isostatic Pressing (HIP) on the studied specimens in this work in 2020.

Appendix A. Supplementary data

Supplementary data to this article can be found online at https://doi.org/10.1016/j.ijfatigue.2025.109447.

Data availability

Data will be made available on request.

References

[1] Advanced Materials - 2024 - Noronha - Titanium Multi-Topology Metamaterials with Exceptional Strength.pdf n.d.
[2] Benedetti M, du Plessis A, Ritchie RO, Dallago M, Razavi N, Berto F. Architected cellular materials: a review on their mechanical properties towards fatigue-tolerant design and fabrication. Mater Sci Eng R Reports 2021;144:100606. https://doi.org/10.1016/j.mser.2021.100606.
[3] Gibson LJ, Editor G. C ellular Solids. Mater Res Soc 2021:270–4.
[4] Kapfer SC, Hyde ST, Mecke K, Arns CH, Schröder-Turk GE. Minimal surface scaffold designs for tissue engineering. Biomaterials 2011;32:6875–82. https://doi.org/10.1016/j.biomaterials.2011.06.012.
[5] Rajagopalan S, Robb RA. Schwarz meets Schwann: Design and fabrication of biomorphic and durataxic tissue engineering scaffolds. Med Image Anal 2006;10:693–712. https://doi.org/10.1016/j.media.2006.06.001.
[6] Yan C, Hao L, Hussein A, Young P. Ti-6Al-4V triply periodic minimal surface structures for bone implants fabricated via selective laser melting. J Mech Behav Biomed Mater 2015;51:61–73. https://doi.org/10.1016/j.jmbbm.2015.06.024.
[7] Castro APG, Pires T, Santos JE, Gouveia BP, Fernandes PR. Permeability versus design in TPMS scaffolds. Materials (Basel) 2019;12. https://doi.org/10.3390/ma12081313.
[8] Leirmo TS, Martinsen K. Deterministic part orientation in additive manufacturing using feature recognition. Procedia CIRP 2020;88:405–10. https://doi.org/10.1016/j.procir.2020.05.070.
[9] Dareh Baghi A, Nafisi S, Hashemi R, Ebendorff-Heidepriem H, Ghomashchi R. Experimental realisation of build orientation effects on the mechanical properties of truly as-built Ti-6Al-4V SLM parts. J Manuf Process 2021;64:140–52. https://doi.org/10.1016/j.jmapro.2021.01.027.
[10] Dong Z, Liu Y, Li W, Liang J. Orientation dependency for microstructure, geometric accuracy and mechanical properties of selective laser melting AlSi10Mg lattices. J Alloy Compd 2019;791:490–500. https://doi.org/10.1016/j.jallcom.2019.03.344.
[11] Amin Yavari S, Ahmadi SM, Wauthle R, Pouran B, Schrooten J, Weinans H, et al. Relationship between unit cell type and porosity and the fatigue behavior of selective laser melted meta-biomaterials. J Mech Behav Biomed Mater 2015;43:91–100. https://doi.org/10.1016/j.jmbbm.2014.12.015.
[12] Yadroitsev I, Krakhmalev P, Yadroitsava I, Johansson S, Smurov I. Energy input effect on morphology and microstructure of selective laser melting single track from metallic powder. J Mater Process Technol 2013;213:606–13. https://doi.org/10.1016/j.jmatprotec.2012.11.014.
[13] Jamshidinia M, Wang L, Tong W, Ajlouni R, Kovacevic R. Fatigue properties of a dental implant produced by electron beam melting® (EBM). J Mater Process Technol 2015;226:255–63. https://doi.org/10.1016/j.jmatprotec.2015.07.013.
[14] Murchio S, Du Plessis A, Luchin V, Maniglio D, Benedetti M. Influence of mean stress and building orientation on the fatigue properties of sub-unital thin-strut miniaturized Ti6Al4V specimens additively manufactured via Laser-Powder Bed Fusion. Int J Fatigue 2024;180:108102. https://doi.org/10.1016/j.ijfatigue.2023.108102.
[15] Murchio S, Dallago M, Zanini F, Carmignato S, Zappini G, Berto F, et al. Additively manufactured Ti–6Al–4V thin struts via laser powder bed fusion: effect of building orientation on geometrical accuracy and mechanical properties. J Mech Behav Biomed Mater 2021;119:104495. https://doi.org/10.1016/j.jmbbm.2021.104495.
[16] Wauthle R, Vrancken B, Beynaerts B, Jorissen K, Schrooten J, Kruth J-P, et al. Effects of build orientation and heat treatment on the microstructure and mechanical properties of selective laser melted Ti6Al4V lattice structures. Addit Manuf 2015;5:77–84. https://doi.org/10.1016/J.ADDMA.2014.12.008.
[17] Weißmann V, Bader R, Hansmann H, Laufer N. Influence of the structural orientation on the mechanical properties of selective laser melted Ti6Al4V open-porous scaffolds. Mater Des 2016;95:188–97. https://doi.org/10.1016/j.matdes.2016.01.095.
[18] Xu Z, Tvenning T, Wu T, Razavi N. Evaluating quasi-static and fatigue performance of IN718 gyroid lattice structures fabricated via LPBF: Exploring relative densities. Int J Fatigue 2024;178:108028. https://doi.org/10.1016/j.ijfatigue.2023.108028.
[19] Kelly CN, Francovich J, Julmi S, Safranski D, Guldberg RE, Maier HJ, et al. Fatigue behavior of As-built selective laser melted titanium scaffolds with sheet-based gyroid microarchitecture for bone tissue engineering. Acta Biomater 2019;94:610–26. https://doi.org/10.1016/j.actbio.2019.05.046.
[20] Alaña M, Cutolo A, Ruiz de Galarreta S, Van Hooreweder B. Influence of relative density on quasi-static and fatigue failure of lattice structures in Ti6Al4V produced by laser powder bed fusion. Sci Rep 2021;11:1–15. https://doi.org/10.1038/s41598-021-98631-3.
[21] Zadpoor AA. Mechanical performance of additively manufactured meta-biomaterials. Acta Biomater 2019;85:41–59. https://doi.org/10.1016/j.actbio.2018.12.038.
[22] de Krijger J, Rans C, Van Hooreweder B, Lietaert K, Pouran B, Zadpoor AA. Effects of applied stress ratio on the fatigue behavior of additively manufactured porous biomaterials under compressive loading. J Mech Behav Biomed Mater 2017;70:7–16. https://doi.org/10.1016/j.jmbbm.2016.11.022.
[23] Ahmadi SM, Hedayati R, Li Y, Lietaert K, Tümer N, Fatemi A, et al. Fatigue performance of additively manufactured meta-biomaterials: the effects of topology and material type. Acta Biomater 2018;65:292–304. https://doi.org/10.1016/j.actbio.2017.11.014.
[24] Kolken HMA, Garcia AF, Du Plessis A, Rans C, Mirzaali MJ, Zadpoor AA. Fatigue performance of auxetic meta-biomaterials. Acta Biomater 2021;126:511–23. https://doi.org/10.1016/j.actbio.2021.03.015.
[25] Meshram SD, Vanderhenst E, Cutolo A, Van Hooreweder B. Torsional and axial tension/compression fatigue behavior of Ti-6Al-4V diamond lattices produced by Laser Powder Bed Fusion (LPBF). Int J Fatigue 2026;203:109320. https://doi.org/10.1016/j.ijfatigue.2025.109320.
[26] Raghavendra S, Dallago M, Zanini F, Carmignato S, Berto F, Benedetti M. A probabilistic average strain energy density approach to assess the fatigue strength of additively manufactured cellular lattice materials. Int J Fatigue 2023;172:107601. https://doi.org/10.1016/j.ijfatigue.2023.107601.
[27] De Biasi R, Oztoprak O, Zanini F, Carmignato S, Kollmannsberger S, Benedetti M. Predicting fatigue life of additively manufactured lattice structures using the

image-based Finite Cell Method and average strain energy density. Mater Des 2024;246:113321. https://doi.org/10.1016/j.matdes.2024.113321.
[28] Boniotti L, Beretta S, Patriarca L, Rigoni L, Foletti S. Experimental and numerical investigation on compressive fatigue strength of lattice structures of AlSi7Mg manufactured by SLM. Int J Fatigue 2019;128:105181. https://doi.org/10.1016/j.ijfatigue.2019.06.041.
[29] Collini F, Meneghetti G. Towards a fracture mechanics-based fatigue assessment of lattice structures obtained from additive manufacturing of metallic powders. Mater Des 2024;244:113077. https://doi.org/10.1016/j.matdes.2024.113077.
[30] Echeta I, Feng X, Dutton B, Leach R, Piano S. Review of defects in lattice structures manufactured by powder bed fusion. Int J Adv Manuf Technol 2020;106:2649–68. https://doi.org/10.1007/s00170-019-04753-4.
[31] Wood P, Libura T, Kowalewski ZL, Williams G, Serjouei A. Influences of horizontal and vertical build orientations and post-fabrication processes on the fatigue behavior of stainless steel 316l produced by selective laser melting. Materials (Basel) 2019;12. https://doi.org/10.3390/ma1224203.
[32] Poulin JR, Brailovski V, Terriault P. Long fatigue crack propagation behavior of Inconel 625 processed by laser powder bed fusion: Influence of build orientation and post-processing conditions. Int J Fatigue 2018;116:634–47. https://doi.org/10.1016/j.ijfatigue.2018.07.008.
[33] Maleki E, Bagherifard S, Heydari Astaraee A, Sgarbazzini S, Bandini M, Guagliano M. Application of gradient severe shot peening as a novel mechanical surface treatment on fatigue behavior of additively manufactured AlSi10Mg. Mater Sci Eng A 2023;881:145397. https://doi.org/10.1016/j.msea.2023.145397.
[34] Lhuissier P, de Formanoir C, Martin G, Dendievel R, Godet S. Geometrical control of lattice structures produced by EBM through chemical etching: Investigations at the scale of individual struts. Mater Des 2016;110:485–93. https://doi.org/10.1016/j.matdes.2016.08.029.
[35] Sangid MD, Book TA, Naragani D, Rotella J, Ravi P, Finch A, et al. Role of heat treatment and build orientation in the microstructure sensitive deformation characteristics of IN718 produced via SLM additive manufacturing. Addit Manuf 2018;22:479–96. https://doi.org/10.1016/j.addma.2018.04.032.
[36] Hrabe N, Gnäupel-Herold T, Quinn T. Fatigue properties of a titanium alloy (Ti–6Al–4V) fabricated via electron beam melting (EBM): Effects of internal defects and residual stress. Int J Fatigue 2017;94:202–10. https://doi.org/10.1016/j.ijfatigue.2016.04.022.
[37] Li SJ, Murr LE, Cheng XY, Zhang ZB, Hao YL, Yang R, et al. Compression fatigue behavior of Ti-6Al-4V mesh arrays fabricated by electron beam melting. Acta Mater 2012;60:793–802. https://doi.org/10.1016/j.actamat.2011.10.051.
[38] Maleki E, Bagherifard S, Bandini M, Guagliano M. Surface post-treatments for metal additive manufacturing: Progress, challenges, and opportunities. Addit Manuf 2021;37:101619. https://doi.org/10.1016/j.addma.2020.101619.
[39] du Plessis A, Macdonald E. Hot isostatic pressing in metal additive manufacturing: X-ray tomography reveals details of pore closure. Addit Manuf 2020;34:101191. https://doi.org/10.1016/j.addma.2020.101191.
[40] Krakhmalev P, Vilardell AM, Takata N. Structural integrity I: Static mechanical properties. In: Fundam. Laser Powder Bed Fusion Met. Elsevier; 2021. p. 349–76.
[41] Masuo H, Tanaka Y, Morokoshi S, Yagura H, Uchida T, Yamamoto Y, et al. Influence of defects, surface roughness and HIP on the fatigue strength of Ti-6Al-4V manufactured by additive manufacturing. Int J Fatigue 2018;117:163–79. https://doi.org/10.1016/j.ijfatigue.2018.07.020.
[42] Leuders S, Lieneke T, Lammers S, Tröster T, Niendorf T. On the fatigue properties of metals manufactured by selective laser melting – the role of ductility. J Mater Res 2014;29:1911–9. https://doi.org/10.1557/jmr.2014.157.
[43] Popov V, Katz-Demyanetz A, Garkun A, Muller G, Strokin E, Rosenson H. Effect of Hot Isostatic pressure treatment on the Electron-Beam Melted Ti-6Al-4V specimens. Proc Manuf 2018;21:125–32. https://doi.org/10.1016/j.promfg.2018.02.102.
[44] Chern AH, Nandwana P, Yuan T, Kirka MM, Dehoff RR, Liaw PK, et al. A review on the fatigue behavior of Ti-6Al-4V fabricated by electron beam melting additive manufacturing. Int J Fatigue 2019;119:173–84. https://doi.org/10.1016/j.ijfatigue.2018.09.022.
[45] Kahlin M, Ansell H, Moverare JJ. Fatigue behaviour of notched additive manufactured Ti6Al4V with as-built surfaces. Int J Fatigue 2017;101:51–60. https://doi.org/10.1016/j.ijfatigue.2017.04.009.
[46] Van Hooreweder B, Apers Y, Lietaert K, Kruth JP. Improving the fatigue performance of porous metallic biomaterials produced by Selective Laser Melting. Acta Biomater 2017;47:193–202. https://doi.org/10.1016/j.actbio.2016.10.005.
[47] Park M, Venter MP, Du Plessis A. Simulation of the compression testing of additively manufactured lattice structures using inputs from microcomputed tomography. Mater Des Process Commun 2023. https://doi.org/10.1155/2023/8000727.
[48] Gockel J, Sheridan L, Koerper B, Whip B. The influence of additive manufacturing processing parameters on surface roughness and fatigue life. Int J Fatigue 2019;124:380–8. https://doi.org/10.1016/j.ijfatigue.2019.03.025.
[49] Du Plessis A, Yadroitsev I, Yadroitsava I, Le Roux SG. X-ray microcomputed tomography in additive manufacturing: a review of the current technology and applications. 3D Print Addit Manuf 2018;5:227–47. https://doi.org/10.1089/3dp.2018.0060.
[50] du Plessis A, Razavi N, Berto F. The effects of microporosity in struts of gyroid lattice structures produced by laser powder bed fusion. Mater Des 2020;194:108899. https://doi.org/10.1016/j.matdes.2020.108899.
[51] McDonald SA, Dedreuil-Monet G, Yao YT, Alderson A, Withers PJ. In situ 3D X-ray microtomography study comparing auxetic and non-auxetic polymeric foams under tension. Phys Status Solidi Basic Res 2011;248:45–51. https://doi.org/10.1002/pssb.201083975.
[52] Meille S, Lombardi M, Chevalier J, Montanaro L. Mechanical properties of porous ceramics in compression: on the transition between elastic, brittle, and cellular behavior. J Eur Ceram Soc 2012;32:3959–67. https://doi.org/10.1016/j.jeurceramsoc.2012.05.006.
[53] Lachambre J, Maire E, Adrien J, Choqueuse D. In situ observation of syntactic foams under hydrostatic pressure using X-ray tomography. Acta Mater 2013;61:4035–43. https://doi.org/10.1016/j.actamat.2013.03.017.
[54] Pérez-Sánchez A, Yánez A, Cuadrado A, Martel O, Nuño N. Fatigue behaviour and equivalent diameter of single Ti-6Al-4V struts fabricated by Electron Bean Melting orientated to porous lattice structures. Mater Des 2018;155:106–15. https://doi.org/10.1016/j.matdes.2018.05.066.
[55] Yánez A, Fiorucci MP, Cuadrado A, Martel O, Monopoli D. Surface roughness effects on the fatigue behaviour of gyroid cellular structures obtained by additive manufacturing. Int J Fatigue 2020;138:105702. https://doi.org/10.1016/j.ijfatigue.2020.105702.
[56] Dallago M, Winiarski B, Zanini F, Carmignato S, Benedetti M. On the effect of geometrical imperfections and defects on the fatigue strength of cellular lattice structures additively manufactured via Selective Laser Melting. Int J Fatigue 2019;124:348–60. https://doi.org/10.1016/j.ijfatigue.2019.03.019.
[57] Barnes B, Babamiri BB, Demeneghi G, Soltani-Tehrani A, Shamsaei N, Hazeli K. Quasi-static and dynamic behavior of additively manufactured lattice structures with hybrid topologies. Addit Manuf 2021;48:102466. https://doi.org/10.1016/j.addma.2021.102466.
[58] Qureshi ZA, Addin Burhan Al-Omari S, Elnajjar E, Al-Ketan O, Al-Rub RA. On the effect of porosity and functional grading of 3D printable triply periodic minimal surface (TPMS) based architected lattices embedded with a phase change material. Int J Heat Mass Transf 2022;183:122111. https://doi.org/10.1016/j.ijheatmasstransfer.2021.122111.
[59] Weeger O, Valizadeh I, Mistry Y, Bhate D. Inelastic finite deformation beam modeling, simulation, and validation of additively manufactured lattice structures. Addit Manuf Lett 2023;4:100111. https://doi.org/10.1016/j.addlet.2022.100111.
[60] Michielsen K, Kole JS. Photonic band gaps in materials with triply periodic surfaces and related tubular structures. Phys Rev B 2003;68:115107. https://doi.org/10.1103/PhysRevB.68.115107.
[61] nTop - Engineering design software for the world's most innovative products | nTop available at n.d. https://www.ntop.com/.
[62] Standardization IO for. Mechanical Testing of Metals: Ductility Testing: Compression Test for Porous and Cellular Metals. International Organization for Standardization; 2010.
[63] BSI CEN. BS EN ISO 6892-1: 2019 Metallic materials-Tensile testing Part 1: Methods of test at room temperature. Bristish Stand; 2019.
[64] Yang L, Yan C, Cao W, Liu Z, Song B, Wen S, et al. Compression–compression fatigue behaviour of gyroid-type triply periodic minimal surface porous structures fabricated by selective laser melting. Acta Mater 2019;181:49–66. https://doi.org/10.1016/j.actamat.2019.09.042.
[65] Kadkhodapour J, Montazerian H, Darabi AC, Anaraki AP, Ahmadi SM, Zadpoor AA, et al. Failure mechanisms of additively manufactured porous biomaterials: effects of porosity and type of unit cell. J Mech Behav Biomed Mater 2015;50:180–91. https://doi.org/10.1016/j.jmbbm.2015.06.012.
[66] Singh SP, Bhardwaj T, Shukla M. Lattice modeling and finite element simulation for additive manufacturing of porous scaffolds. 2017 Int Conf Adv Mech Ind Autom Manag Syst 2017:333–6. https://doi.org/10.1109/AMIAMS.2017.8069234.
[67] Mora Sierra DC, Heydari Astaraee A, Guagliano M, Bagherifard S. Numerical investigation of Ti6Al4V gradient lattice structures with tailored mechanical response. Adv Eng Mater 2022;24. https://doi.org/10.1002/adem.202101760.
[68] Dumontet N, Connétable D, Malard B, Viguier B. Elastic properties of the α' martensitic phase in the Ti-6Al-4V alloy obtained by additive manufacturing. Scr Mater 2019;167:115–9. https://doi.org/10.1016/j.scriptamat.2019.03.042.
[69] Standard A. ISO/ASTM 52900: 2015 Additive manufacturing-General principles-terminology. ASTM F2792-10e1; 2012.
[70] Foti P, Razavi N, Benedetti M, du Plessis A, Berto F. 11 - Mechanical properties of lattice materials for fatigue-tolerant design and fabrication. In: Berto F, du Plessis ABT-F in AMM, editors. Fatigue Addit. Manuf. Met., Elsevier; 2024. p. 259–300. doi: 10.1016/B978-0-323-91204-4.00002-2.
[71] Zhang L, Song B, Fu JJ, Wei SS, Yang L, Yan CZ, et al. Topology-optimized lattice structures with simultaneously high stiffness and light weight fabricated by selective laser melting: Design, manufacturing and characterization. J Manuf Process 2020;56:1166–77. https://doi.org/10.1016/j.jmapro.2020.06.005.
[72] Merkt S, Hinke C, Bültmann J, Brandt M, Xie YM. Mechanical response of TiAl6V4 lattice structures manufactured by selective laser melting in quasistatic and dynamic compression tests. J Laser Appl 2015;27. https://doi.org/10.2351/1.4898835.
[73] Maconachie T, Leary M, Tran P, Harris J, Liu Q, Lu G, et al. The effect of topology on the quasi-static and dynamic behaviour of SLM AlSi10Mg lattice structures. Int J Adv Manuf Technol 2022;118:4085–104. https://doi.org/10.1007/s00170-021-08203-y.
[74] Ushijima K, Cantwell WJ, Mines RAW, Tsopanos S, Smith M. An investigation into the compressive properties of stainless steel micro-lattice structures. J Sandw Struct Mater 2011;13:303–29. https://doi.org/10.1177/1099636210380997.
[75] Ling C, Cernicchi A, Gilchrist MD, Cardiff P. Mechanical behaviour of additively-manufactured polymeric octet-truss lattice structures under quasi-static and

dynamic compressive loading. Mater Des 2019;162:106–18. https://doi.org/10.1016/j.matdes.2018.11.035.
[76] Bae S, Mieses AM, Bayrak O. Inelastic Buckling of reinforcing Bars. J Struct Eng 2005;131:314–21. https://doi.org/10.1061/(asce)0733-9445(2005)131:2(314).
[77] Gümrük R, Mines RAW, Karadeniz S. Static mechanical behaviours of stainless steel micro-lattice structures under different loading conditions. Mater Sci Eng A 2013;586:392–406. https://doi.org/10.1016/j.msea.2013.07.070.
[78] Hu B, Wu LZ, Xiong J, Ma L, Yang W, Jin Y. Mechanical properties of a node-interlocking pyramidal welded tube lattice sandwich structure. Mech Mater 2019; 129:290–305. https://doi.org/10.1016/j.mechmat.2018.12.006.
[79] Choy SY, Sun CN, Leong KF, Wei J. Compressive properties of Ti-6Al-4V lattice structures fabricated by selective laser melting: Design, orientation and density. Addit Manuf 2017;16:213–24. https://doi.org/10.1016/j.addma.2017.06.012.
[80] Maskery I, Aboulkhair NT, Aremu AO, Tuck CJ, Ashcroft IA. Compressive failure modes and energy absorption in additively manufactured double gyroid lattices. Addit Manuf 2017;16:24–9. https://doi.org/10.1016/j.addma.2017.04.003.
[81] Maskery I, Aboulkhair NT, Aremu AO, Tuck CJ, Ashcroft IA, Wildman RD, et al. A mechanical property evaluation of graded density Al-Si10-Mg lattice structures manufactured by selective laser melting. Mater Sci Eng A 2016;670:264–74. https://doi.org/10.1016/j.msea.2016.06.013.
[82] Liu C, Xu T, Mao H, Li K, Jing C, Liu B, et al. Quasi-static compressive behaviors of large-size titanium lattice sandwich structure based on pulse hot-wire arc additive manufacturing. Mater Sci Eng A 2023;868:144787. https://doi.org/10.1016/j.msea.2023.144787.
[83] Bai L, Gong C, Chen X, Zheng J, Yang J, Li K, et al. Heterogeneous compressive responses of additively manufactured Ti-6Al-4V lattice structures by varying geometric parameters of cells. Int J Mech Sci 2022;214. https://doi.org/10.1016/j.ijmecsci.2021.106922.
[84] Xiao L, Song W, Wang C, Liu H, Tang H, Wang J. Mechanical behavior of open-cell rhombic dodecahedron Ti-6Al-4V lattice structure. Mater Sci Eng A 2015; 640:375–84. https://doi.org/10.1016/j.msea.2015.06.018.
[85] Wei K, Peng Y, Wang K, Yang F, Cheng S, Zeng T. High temperature mechanical properties of lightweight C/SiC composite pyramidal lattice core sandwich panel. Compos Struct 2017;178:467–75. https://doi.org/10.1016/j.compstruct.2017.07.049.
[86] Zhang L, Feih S, Daynes S, Chang S, Wang MY, Wei J, et al. Energy absorption characteristics of metallic triply periodic minimal surface sheet structures under compressive loading. Addit Manuf 2018;23:505–15. https://doi.org/10.1016/j.addma.2018.08.007.
[87] Yan C, Hao L, Hussein A, Raymont D. Evaluations of cellular lattice structures manufactured using selective laser melting. Int J Mach Tool Manuf 2012;62:32–8. https://doi.org/10.1016/j.ijmachtools.2012.06.002.
[88] Zhu G, Wen D, Wei L, Wang Z, Zhao X. Mechanical performances of novel cosine function cell-based metallic lattice structures under quasi-static compressive loading. Compos Struct 2023;314:116962. https://doi.org/10.1016/j.compstruct.2023.116962.
[89] Gümrük R, Mines RAW. Compressive behaviour of stainless steel micro-lattice structures. Int J Mech Sci 2013;68:125–39. https://doi.org/10.1016/j.ijmecsci.2013.01.006.
[90] Novak N, Al-Ketan O, Krstulović-Opara L, Rowshan R, Abu Al-Rub RK, Vesenjak M, et al. Quasi-static and dynamic compressive behaviour of sheet TPMS cellular structures. Compos Struct 2021;266:1–10. https://doi.org/10.1016/j.compstruct.2021.113801.
[91] Yan C, Hao L, Hussein A, Young P, Raymont D. Advanced lightweight 316L stainless steel cellular lattice structures fabricated via selective laser melting. Mater Des 2014;55:533–41. https://doi.org/10.1016/j.matdes.2013.10.027.
[92] du Plessis A, Razavi N, Benedetti M, Murchio S, Leary M, Watson M, et al. Properties and applications of additively manufactured metallic cellular materials: a review. Prog Mater Sci 2022;125:100918. https://doi.org/10.1016/j.pmatsci.2021.100918.
[93] Ashby MF, Evans T, Fleck NA, Hutchinson JW, Wadley HNG, Gibson LJ. Metal foams: a design guide. Elsevier; 2000.
[94] Mahmoud D, Al-Rubaie KS, Elbestawi MA. The influence of selective laser melting defects on the fatigue properties of Ti6Al4V porosity graded gyroids for bone implants. Int J Mech Sci 2021;193. https://doi.org/10.1016/j.ijmecsci.2020.106180.
[95] Amin Yavari S, Wauthle R, Van Der Stok J, Riemslag AC, Janssen M, Mulier M, et al. Fatigue behavior of porous biomaterials manufactured using selective laser melting. Mater Sci Eng C 2013;33:4849–58. https://doi.org/10.1016/j.msec.2013.08.006.
[96] Ahmadi SM, Kumar R, Borisov EV, Petrov R, Leeflang S, Li Y, et al. From microstructural design to surface engineering: a tailored approach for improving fatigue life of additively manufactured meta-biomaterials. Acta Biomater 2019; 83:153–66. https://doi.org/10.1016/j.actbio.2018.10.043.
[97] Soro N, Saintier N, Merzeau J, Veidt M, Dargusch MS. Quasi-static and fatigue properties of graded Ti–6Al–4V lattices produced by Laser Powder Bed Fusion (LPBF). Add Manuf 2021;37:101653. https://doi.org/10.1016/j.addma.2020.101653.
[98] Hrabe NW, Heinl P, Flinn B, Körner C, Bordia RK. Compression-compression fatigue of selective electron beam melted cellular titanium (Ti-6Al-4V). J Biomed Mater Res - Part B Appl Biomater 2011;99 B:313–20. https://doi.org/10.1002/jbm.b.31901.
[99] Wu MW, Chen JK, Lin BH, Chiang PH. Improved fatigue endurance ratio of additive manufactured Ti-6Al-4V lattice by hot isostatic pressing. Mater Des 2017;134:163–70. https://doi.org/10.1016/j.matdes.2017.08.048.
[100] Wu MW, Chen JK, Lin BH, Chiang PH, Tsai MK. Compressive fatigue properties of additive-manufactured Ti-6Al-4V cellular material with different porosities. Mater Sci Eng A 2020;790:139695. https://doi.org/10.1016/j.msea.2020.139695.
[101] Cain V, Thijs L, Van Humbeeck J, Van Hooreweder B, Knutsen R. Crack propagation and fracture toughness of Ti6Al4V alloy produced by selective laser melting. Add Manuf 2015;5:68–76. https://doi.org/10.1016/j.addma.2014.12.006.
[102] Yang J, Yu H, Wang Z, Zeng X. Effect of crystallographic orientation on mechanical anisotropy of selective laser melted Ti-6Al-4V alloy. Mater Charact 2017;127:137–45. https://doi.org/10.1016/j.matchar.2017.01.014.
[103] Yuan W, Hou W, Li S, Hao Y, Yang R, Zhang LC, et al. Heat treatment enhancing the compressive fatigue properties of open-cellular Ti-6Al-4V alloy prototypes fabricated by electron beam melting. J Mater Sci Technol 2018;34:1127–31. https://doi.org/10.1016/j.jmst.2017.12.003.
[104] 1993-1-3:2009 BE. Eurocode 3: Design of steel structures - Part 1-9: Fatigue. Eurocode 3 Des. steel Struct. - Part 1-9 Fatigue, vol. 7; 2011.
[105] Razavi N, Van Hooreweder B, Berto F. Effect of build thickness and geometry on quasi-static and fatigue behavior of Ti-6Al-4V produced by electron beam melting. Addit Manuf 2020;36:101426. https://doi.org/10.1016/j.addma.2020.101426.
[106] Yu H, Li F, Wang Z, Zeng X. Fatigue performances of selective laser melted Ti-6Al-4V alloy: Influence of surface finishing, hot isostatic pressing and heat treatments. Int J Fatigue 2019;120:175–83. https://doi.org/10.1016/j.ijfatigue.2018.11.019.
[107] Sanaei N, Fatemi A. Analysis of the effect of internal defects on fatigue performance of additive manufactured metals. Mater Sci Eng A 2020;785:139385. https://doi.org/10.1016/j.msea.2020.139385.
[108] Yang L, Wu S, Yan C, Chen P, Zhang L, Han C, et al. Fatigue properties of Ti-6Al-4V Gyroid graded lattice structures fabricated by laser powder bed fusion with lateral loading. Addit Manuf 2021;46:102214. https://doi.org/10.1016/j.addma.2021.102214.
[109] Yánez A, Cuadrado A, Martel O, Afonso H, Monopoli D. Gyroid porous titanium structures: a versatile solution to be used as scaffolds in bone defect reconstruction. Mater Des 2018;140:21–9. https://doi.org/10.1016/j.matdes.2017.11.050.
[110] Chen JK, Wu MW, Cheng TL, Chiang PH. Continuous compression behaviors of selective laser melting Ti-6Al-4V alloy with cuboctahedron cellular structures. Mater Sci Eng C 2019;100:781–8. https://doi.org/10.1016/j.msec.2019.03.054.
[111] Pyka BG, Burakowski A, Kerckhofs G, Moesen M, Van BS, Schrooten J, et al. Surface modification of Ti6Al4V open porous structures produced by additive manufacturing. Adv Eng Mater 2012:363–70. https://doi.org/10.1002/adem.201100344.
[112] Yavari SA, Ahmadi SM, Van Der SJ, Wauthle R. Effects of bio-functionalizing surface treatments on the mechanical behavior of open porous titanium biomaterials. J Mech Behav Biomed Mater 2014;36:109–19. https://doi.org/10.1016/j.jmbbm.2014.04.010.